國立臺灣大學工學院土木工程研究所

碩士論文

Department of Civil Engineering

College of Engineering

National Taiwan University

Master's Thesis

以物理引導之生成式 AI 預測 RC 橋柱破壞模式與遲滯行為

Physics-guided Generative AI for Hysteretic Behavior Prediction and Failure Forecasting in RC Bridge Columns

吳亭諺

Ting-Yan Wu

指導教授: 吳日騰 博士

Advisor: Rih-Teng Wu, Ph.D.

中華民國 113 年 7 月

July, 2024

doi:10.6342/NTU202402878

國立臺灣大學碩士學位論文
口試委員會審定書

NATIONAL TAIWAN UNIVERSITY
MASTER'S THESIS ACCEPTANCE CERTIFICATE

以物理引導之生成式AI預測RC橋柱破壞模式與遲滯行為

Physics-guided Generative AI for Hysteretic Behavior Prediction and Failure Forecasting in RC Bridge Columns

本論文係 吳亭諺 (R11521607) 在國立臺灣大學土木工程學系電腦輔助工程組完成之碩士學位論文，於民國113年07月26日承下列考試委員審查通過及口試及格，特此證明。

The undersigned, appointed by the Department of Civil Engineering Computer-Aided Engineering on July 26, 2024 have examined a Master's Thesis entitled above presented by Ting-Yan Wu (R11521607) candidate and hereby certify that it is worthy of acceptance.

口試委員 Oral examination committee:

吳日騰 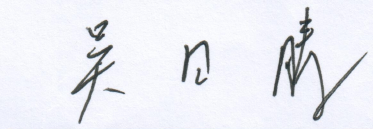

（指導教授 Advisor）

歐昱辰 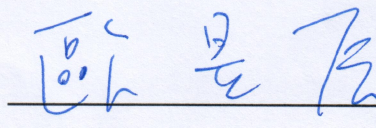

張國鎮 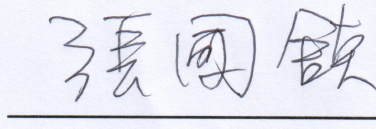

宋裕祺 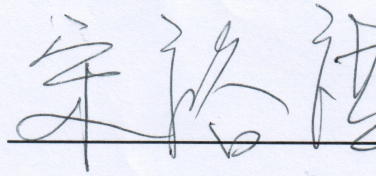

系主管 Director： 葛宇甯 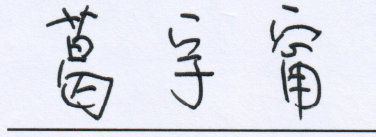

Acknowledgements

本論文得以完成，首先要感謝我的指導教授吳日騰教授。在我大四推甄上研究生後，便開始指導我進行研究。雖然自己在大學時期已有一些專題經驗，但對於研究的發想及方法仍感到十分生疏。教授不厭其煩地幫助我釐清研究方向，並在整個研究過程中細心指導，使自己逐漸掌握了研究的流程。這些寶貴的指導讓我後續的研究能夠順利進行，並且能夠獨立完成自己的研究工作。教授還多次讓我參加國內外研討會，讓自己有機會學習如何在公開場合呈現自己的研究成果。衷心感謝在碩士期間能夠遇到我的指導老師。也十分感謝在論文口試時願意擔任口委的張國鎮教授、歐昱辰教授及宋裕祺教授，教授們的指教皆使我的論文更加完整。

此外，很榮幸自己身為 MarCE Lab 的一員，由於進入研究室時正值草創階段，自己有了許多機會學習到研究以外的知識。例如，如何架設及管理研究室伺服器及網站，如何與廠商溝通協商，以及學校的採購流程等。這些經歷豐富了我這兩年的研究生活。感謝研究室同屆夥伴海威、泓博、泓瑋、家文、宥維、揚升一路陪伴，一起學習並提供各自研究上不同建議。身為第二屆的我們希望有好好地為學弟妹建立起良好的研究室文化，也期許 MarCE Lab 能繼續蓬勃發展。

另外，也要感謝我的家人們在這兩年給我的支持，感謝爸媽、姐姐及阿嬤日常的照顧給我在學校的任何建議，有了這些我才能無憂無慮的進行研究。雖然阿

doi:10.6342/NTU202402878

嬤沒辦法在最後見證畢業這一刻，希望自己這兩年的成果沒有辜負家人及阿嬤的期待。最後也感謝伽映及厚片在無數夜晚的陪伴，讓我在研究的過程中能獲得許多前進的動力。回顧這兩年的艱辛歲月，雖然充滿挑戰，但也真切地感受到自身的顯著成長。藉此向所有支持及幫助我的人表達最誠摯的敬意和感謝。

doi:10.6342/NTU202402878

摘要

對地震工程而言，鋼筋混凝土 (Reinforcement Concrete, RC) 橋柱的遲滯行為、損壞機制及結構性能指標如損害指數（Damage Index, DI）可以提供工程師了解橋柱在反覆載重下的反應行為，因此如何在設計階段時獲取橋柱的遲滯行為及損壞機制是當今重要的研究課題。本研究提出了一個基於閘門循環單元（Gated Recurrent Unit, GRU）的遲滯迴圈預測網路 (HysGRU)，旨在彌平有限元模擬和真實實驗之間的差異。經由實驗，在模擬所提供的物理限制下，HysGRU 達到了 31.51 kN 的均方根誤差，相較於純粹數據驅動的方法和模擬所獲得之誤差，分別降低了 24%和 62%。此外，HysGRU 於預測遲滯迴圈時，也會一併提取每個層間位移角 (Drift Ratio) 下所對應之潛在特徵，於此研究中，此潛在特徵作為所提出的損傷模式生成模型 HysGAN 之條件，藉由輸入不同時間點之潛在特徵以控制 HysGAN 生成每個層間位移角下相對應的損傷影像。為了評估 HysGAN 的模型表現，此研究亦額外提出了一個損傷指標預測網路，透過預測生成之損傷影像對應之損傷指標，計算預測與真實值之間的 R^2 分數，藉此評估模型生成表現。HysGAN 在驗證和測試數據集上皆可達到 0.92 的 R^2 分數，相對於基準模型，分別增加了 0.05 和 0.55，顯示出經由潛在特徵的控制可以有效提升模型的通用性及生成影像之品質。此研究中所提出之橋柱損害預測框架可以提供工程師根據設計預定之柱設計參數，預測設計橋柱之遲滯行為，並可以透過選定特定層間位移角，觀察橋柱破壞形式，使工程師可以更有效評估設計橋柱在反覆載重下之結構

doi:10.6342/NTU202402878

行為。

關鍵字：結構性能設計、生成式人工智慧、損壞模式預測、閘門循環單元、遲滯行為預測、條件圖像生成

doi:10.6342/NTU202402878

Abstract

Seismic attributes of reinforced concrete (RC) bridge columns, including hysteretic response, damage mechanism, and structural performance measures such as the Damage Index (DI), are pivotal to the domain of seismic engineering. In this study, a sequence-to-sequence hysteresis prediction network based on Gated Recurrent Units (GRU), HysGRU, is proposed to bridge the discrepancy between finite element simulation and experiment. Guided by the physics constraints extrapolated from simulation, HysGRU achieves a root mean square error (RMSE) of 31.51 kN, representing a reduction of 24% and 62% compared to the purely data-driven methodology and simulation, respectively. Moreover, during the prediction of HysGRU, the physics features of hysteretic behavior are extracted as a condition of the proposed damage pattern generative model, HysGAN, which is based on a conditional generative adversarial network (CGAN). To evaluate the performance of HysGAN, a DI prediction network is proposed to assess R^2 scores by the DI prediction of the synthetic damage patterns. Comprehensive experimental evaluations have demon-

doi:10.6342/NTU202402878

strated that the integration of latent feature conditioning substantially enhances the quality, stability, and generalization performance. HysGAN attains R^2 scores of 0.92 for both the validation and test datasets, representing significant improvements over the baseline model, with increases of 0.05 and 0.55, respectively. The proposed prognostic framework enables engineers to delineate the hysteresis loop and damage patterns based on predefined column design parameters and chosen drift ratios, facilitating an efficient assessment of seismic design and structural capacity.

Keywords: Performance-based design, Generative AI, Damage Patterns Forecasting, Gated Recurrent Unit, Hysteresis Behavior Prediction, Conditional Image Generation

doi:10.6342/NTU202402878

Contents

doi:10.6342/NTU202402878

doi:10.6342/NTU202402878

doi:10.6342/NTU202402878

List of Figures

doi:10.6342/NTU202402878

doi:10.6342/NTU202402878

doi:10.6342/NTU202402878

List of Tables

doi:10.6342/NTU202402878

doi:10.6342/NTU202402878

Chapter 1 Introduction

Bridge systems are essential components of infrastructure that enable safe and efficient transportation across obstacles such as rivers, valleys, and roadways. The structural integrity and stability of these bridges become particularly critical in regions prone to seismic activity, with the design and robustness of bridge columns are crucial in sustaining such stability. In seismic events, bridge columns are designed to absorb and dissipate energy through controlled flexure and deformation, thereby avoiding catastrophic failure. Consequently, it becomes imperative to assess the performance of bridge columns following extreme events, underscoring the importance of performance-based design [1]. This methodology delineates desirable structural design criteria based on achieving specific performance objectives under various hazards, contrasting with the conventional strength-based design approach that focuses solely on ultimate strength capacity. The performance-based design approach considers various performance levels, thereby offering a more exhaustive evaluation of structural behavior under different conditions. By embedding performance objectives into the design process, engineers can estimate the residual service life of a structure after natural hazards or extreme events. This design approach not only increases the resilience and safety of bridge systems, but also ensures the enduring functionality and reliability of RC bridge columns.

Cyclic loading tests on RC bridge columns are essential, particularly in terms of struc-

doi:10.6342/NTU202402878

tural performance and safety under conditions that mimic real-world scenarios such as seismic events and traffic-induced loads. The applied loading changes the direction cyclically during cyclic loading tests, allowing engineers to assess the seismic performance of RC bridge columns. These evaluations are essential for understanding the behavior of columns under repeated load reversals, which is critical to determine the resilience and ductility of bridge columns. In addition, understanding the degradation of columns under cyclic loading helps in forecasting the lifespan and maintenance requirements. These tests also clarify the failure mechanisms of RC columns under cyclic loading. Identifying how and where columns are likely to fail informs improved design and reinforcement strategies to enhance durability and safety. For existing bridges, cyclic loading tests can assess the efficacy of various retrofit strategies, which is crucial to upgrade older structures to contemporary safety standards without the need for complete reconstruction. Under cyclic loads, RC columns exhibit nonlinear behaviors such as cracking, yielding, and strain hardening. Testing under these conditions aids engineers in developing more precise analytical models to predict column performance in actual service conditions.

During cyclic loading tests, hysteresis loops can be obtained to describe the relationship between applied force and resulting displacement. By examining hysteresis loops, engineers can assess the energy dissipation capacity of RC bridge columns, an essential factor in evaluating ductility and the ability to withstand repeated seismic forces without significant strength loss. Various approaches, including numerical analysis[2][3], laboratory experiments[4][5], and in-situ tests[6][7], are commonly adopted to observe or simulate hysteretic behavior in RC columns. Numerical analysis provides a cost-effective and efficient way to predict RC bridge column responses, which aids in detailed parametric studies and simulations under various loading conditions. Nevertheless, simulations

doi:10.6342/NTU202402878

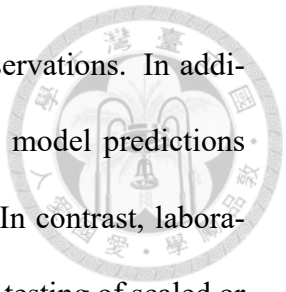

often exhibit significant discrepancies compared to experimental observations. In addition, numerical approaches lack the capacity to accurately correlate model predictions with physical damage patterns encountered in real-world scenarios. In contrast, laboratory and in-situ experiments yield empirical data through the physical testing of scaled or full-scale specimens. These experiments monitor the structural response and document the damage behavior. However, such experimental procedures are labor intensive and time-consuming, precluding the feasibility of testing across a broad spectrum of design parameters. Given the limitations of each method, it is imperative to develop novel and effective methodologies to predict hysteretic behavior.

Beyond hysteretic behavior, the damage pattern in RC columns is another crucial factor in evaluating structural performance, especially in terms of seismic resilience. By precisely predicting how RC columns will visually deteriorate under stress, engineers can pinpoint potential failure locations and evaluate the overall integrity of the structure. Numerical simulation techniques are often employed to perform damage analysis of RC columns subjected to cyclic loading or seismic responses. However, the simulated outcomes are confined within the model itself and cannot be directly correlated to the actual damaged scenario. Therefore, there is an urgent need to develop a comprehensive framework for predicting the hysteretic behavior and damage patterns of RC bridge columns independently of experimental data. Such a framework would be an efficient tool for assessing the structural performance of design proposals, thereby determining the feasibility of the design.

doi:10.6342/NTU202402878

1.1 Literature Review

The precise prediction of the hysteresis loop for RC columns is crucial to evaluating the inelastic seismic behavior of structures. Traditionally, techniques such as finite element modeling and numerical analysis are commonly used to assess hysteresis behavior [8][9][10]. Hao et al. [11] complemented the finite element analysis to clarify the impact of the analyzed parameters. The ABAQUS finite element software was employed to construct the finite element model and to further evaluate the influence of the investigated parameters. Nevertheless, these methodologies require the adjustment of parameters and assumptions based on experimental data, which may be specifically customized to specific scenarios. On the other hand, numerical analysis can also be utilized to describe the hysteretic behavior. The Bouc-Wen-Baber-Noori (BWBN) model [12][13][14] constitutes a significant enhancement to the original Bouc-Wen framework, which is a hysteretic model typically utilized to characterize non-linear hysteretic systems. The governing equation of the BWBN model is formulated based on the correlation between the inelastic restoring force and the lateral displacement. Consequently, to model the hysteretic behavior, numerous studies have been dedicated to the identification of the parameters of the BWBN model. Ma et al. [15] proposed an advanced parameter identification methodology within the framework of the BWBN model relevant to RC columns. The resultant parameterized BWBN model exhibits a remarkable degree of precision in modeling the hysteresis loops characteristic of RC columns. These methodologies construct the model of bridge column that enables the application of advanced seismic analyses. Nonetheless, there remains a critical necessity to formulate a methodology capable of accurately predicting hysteretic behavior in the absence of experimental data.

doi:10.6342/NTU202402878

With the emergence of deep learning [16], there has been a surge in research exploring the use of deep learning to approximate the structural response of structural components[17][18][19][18]. DL algorithms have the ability to learn from observed cases and approximate the structural response of unobserved cases. Ning et al. [20] proposed an Artificial Neural Network (ANN) to evaluate the parameters of the BWBN model. Incorporating column design parameters, the ANN forecasts the corresponding BWBN parameters, thereby enabling the modeling of the hysteresis loop using the forecasted parameters. However, identifying the BWBN parameters before training is time-consuming; therefore, it is essential to develop a methodology for predicting the sequential behavior of RC columns throughout the entire non-linear hysteresis period. However, there is a lack of research to predict the entire hysteresis response sequentially. To address this issue, Recurrent Neural Network (RNN) based models are designed to deal with the sequential data by iterative computation.

RNNs are a class of artificial neural networks designed to effectively process sequential data by maintaining a hidden state that captures information about previous inputs. This capability makes RNNs particularly powerful for tasks such as speech recognition [21][22][23], language modeling [24][25][26], and time series prediction [27][28][29]. In recent years, many researchers in civil engineering have adopted RNNs to predict structural response [30][31][32][33]. Ni et al. [34] introduced a Recurrent Neural Network model using Long Short-term Memory (LSTM) and Gated Recurrent Units (GRU) to predict the strength related to the temporal sequence, taking into account multiple variables. Nevertheless, the database of the study was based on only six specimens, which could limit the generalization capability of the model. Furthermore, parts of the experimental hysteresis responses of each sample were utilized as training samples, while the model

doi:10.6342/NTU202402878

validation was performed on the rest of the data. However, in the RC column design process, it is not able to access any information about experimental hysteretic behavior. Consequently, it is imperative to develop a methodology that enables the direct prediction of the entire hysteresis loop.

However, directly predicting the hysteresis behavior of bridge columns may be challenged with the constraint of limited data availability. Physics-guided training leverages advanced deep learning models to statistically infer established physics principles through the extraction of features and attributes from data obtained via rigorously controlled experimental procedures and computational analysis [35]. As a result, accurately predicting the entire hysteresis behavior with incorporation of physics information is crucial, even without any prior knowledge of experimental hysteresis information.

Beyond hysteretic behavior, the damage patterns in RC columns serve as crucial indicators for assessing structural performance, particularly with regard to seismic resilience. By accurately forecasting how RC columns will visually degrade under stress, engineers can identify potential failure points and assess the overall health of the structure. Numerical simulation methods are often adopted to perform damage analysis of RC columns under cyclic loading or seismic responses [36][37][38][39][40]. Gao et al. [41] employed a fiber beam–column element model to simulate and analyze quasi-static tests of RC columns. This advanced fiber element model reliably predicts the non-linear mechanical behavior and damage distribution of RC columns with high accuracy. Saritas and Filippou [2] presents a methodology for incorporating a suite of plastic-damage material models within the finite element framework to determine the strain and stress distributions in columns, subsequently clarifying both tensile and compressive damage. Nevertheless, the outcomes derived from finite element model (FEM) remain confined to the simula-

doi:10.6342/NTU202402878

tion environment and lack direct correlation with real damage scenarios. In this study, we attempt to address this challenge by utilizing deep learning algorithms.

Generative Adversarial Network (GAN) [42] represents a class of deep learning algorithms initially developed to generate synthetic images. A GAN comprises a generator tasked with synthesizing data that closely resemble authentic data, and a discriminator designed to differentiate between authentic and synthetic data. By exploiting the adversarial training paradigm, the generator and the discriminator attain a state of equilibrium. Consequently, the generator, upon completion of training, acquires the capability to generate synthetic data. To facilitate the detection of internal defects such as delamination, debonding, cracks, voids, and honeycombing, Ali and Cha [43] generate thermographic data to enhance the efficacy of internal damage segmentation through the deployment of an attention-based GAN. Furthermore, Shim et al. [44] employ a GAN to reconstruct low-resolution images, thereby augmenting the efficacy of pavement damage detection.

It is noteworthy that a conventional GAN model solely employs random noise as input to synthesize images, leading to a lack of correlation between the generated images and any specific parameters. To mitigate this limitation, the Conditional Generative Adversarial Network (CGAN) [45] is designed to generate images conditioned on particular parameters. In contrast to a standard GAN, the CGAN integrates supplementary conditional variables, specifically the label information, into both the generator and the discriminator during the training phase. This label information may encompass a categorical classification or a parameter associated with the authentic dataset. Upon the completion of training, the CGAN is capable of generating synthetic data control by a specified condition in conjunction with random noise. This capability is especially advantageous for generating synthetic datasets from particular classes or with specific physics parameters.

doi:10.6342/NTU202402878

Zhang et al. [46] introduce Defect-GAN, an innovative approach that transforms standard surface images into synthesized defect images. By employing spatial and categorical maps as conditional inputs, Defect-GAN can generate specific types of damage at designated locations, resulting in high-fidelity surface defect images. However, the main focus of the existing research is largely on increasing the quantity of the dataset. As a result, our previous work [47] developed a CGAN for high-fidelity prediction of RC column failure, which can predict the damage patterns according to design parameters and performance indicators. However, the performance indicators are calculated by the hysteresis loop assessed by laboratory cyclic loading experiments, which means that the results of experiments are still required. Moreover, the predictive process lacks data pertaining to the hysteretic behavior of bridge columns, which is critical for understanding the degradation mechanisms of these structural elements. Hence, it is urgent to develop a comprehensive framework damage patterns forecast approach leveraging information from hysteresis loop.

Within the operational lifespan of a bridge, it is imperative to conduct a thorough evaluation of the seismic damage sustained by RC structures to ensure their safety. Employing damage models for the quantitative assessment of seismic damage is vital for clarifying the failure mechanisms inherent in RC structures. Park and Ang [48] pioneered the development of a model for seismic damage assessment in RC structures, incorporating both maximum deformation and the effects of repeated cyclic loading through a linear functional approach. Ideally, the quantification of these damage models should be predicated upon the analysis of the hysteresis loop; however, accurately evaluating the hysteretic behavior of extant structures often presents substantial challenges. As a result, extensive research is dedicated to vision-based seismic damage recognition, which presents a

doi:10.6342/NTU202402878

promising alternative for assessing structural integrity by utilizing visual data and sophisticated image processing methodologies. Xu et al. [49] proposed an advanced framework for the detection of seismic damage, involving phenomena such as cracks, spalling, and rebar exposure. By integrating the detected damage with column design specifications, a regression network was formulated to derive the corresponding damage indices. These vision-based networks facilitate the direct evaluation of seismic damage post-earthquake through the utilization of damage imagery, eliminating the need for detailed knowledge of structural hysteretic behavior.

1.2 Research Objective and Contribution

To address the aforementioned challenges, this study proposes an advanced framework that integrates computer vision and deep learning techniques to prognosticate damage patterns and hysteresis loops to evaluate the seismic characteristics and failure mechanisms of the RC bridge columns. First, we propose a finite element simulation process to obtain the simulated hysteresis loops, which is developed to derive the physics constraints for guiding deep learning networks. To bridge the discrepancy between simulation and experiment, we propose a Gated Recurrent Unit (GRU)-based network, HysGRU, to predict hysteresis loops by leveraging simulation results to forecast actual hysteresis behavior within the constraints of numerical simulations. Guided by the prior physics knowledge derived from the simulation outcomes, the proposed HysGRU model integrates these physics by incorporating the simulation data during the predictive process of the corresponding hysteresis loops. Furthermore, to generate the corresponding damage patterns throughout the entirety of the hysteresis loop, HysGRU extracts informative latent features from the respective drift ratio steps, which subsequently serve as conditional

doi:10.6342/NTU202402878

inputs for the proposed generative model, HysGAN. In assessing the damage patterns, it is crucial to evaluate the consistency of column degradation. Nevertheless, traditional similarity metrics like peak signal-to-noise ratio (PSNR), structural similarity index (SSIM), and Fréchet Inception Distance (FID) are proved inadequate to fully quantify the consistency of synthetic damage patterns, given the complex mechanism of damage of bridge columns. Consequently, we introduce a vision-based network for predicting the Damage Index (DI), which is trained using authentic data. Subsequently, this network is employed to compute the coefficient of determination (R^2) for the corresponding synthetic data to determine the efficacy of HysGAN. The proposed framework provides engineers with the capability to evaluate hysteresis behavior and visualize damage patterns in accordance with the design specifications. This facilitates the assessment of structural performance, enabling the attainment of defined performance objectives. In the seismic events that result in noticeable damage to bridge columns, the developed DI prediction network remains proficient at evaluating residual structural performance, thereby providing engineers with a reliable decision-making instrument. The contribution of this work is concisely presented as follows:

- We establish the hysteresis database utilizing the open-access PEER structural performance database and extract comprehensive sectional data from the original documentation associated with each specimen.

- An automatically simulation process is proposed to simulate the hysteretic behavior of RC columns and provide physics constraints for guiding the proposed HysGRU.

- The proposed HysGRU model demonstrates the capability to accurately forecast the hysteretic response of RC bridge columns. Leveraging the physics constraints

doi:10.6342/NTU202402878

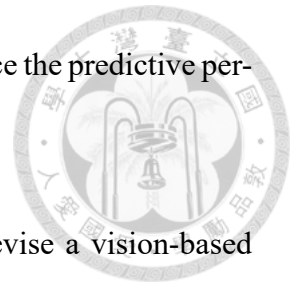

embedded within the simulation results can substantially enhance the predictive performance of the HysGRU model.

- To assess the effectiveness of the generated outcomes, we devise a vision-based Damage Index (DI) prediction network that estimates the DI utilizing the identified damage patterns alongside column design parameters.

- Latent features encapsulating physics-based information are extracted by the HysGRU, subsequently serving as condition inputs for the HysGAN to synthesize corresponding damage patterns for all time steps in the hysteresis loop. Through comprehensive experiments, latent features conditioning enhances the quality and generalizability of HysGAN.

1.3 Scope of Thesis

This study proposes a prognostic framework that integrates an automated simulation process, HysGRU, HysGAN, and the DI prediction network. This thesis will thoroughly introduce these components, with the structure organized as follows: Chapter 2 introduces the database, including the hysteresis database and the damage pattern database. The details of the data acquisition process are elaborated. In Chapter 3, the proposed automatic simulation methodologies, HysGRU, HysGAN, and the DI prediction network are thoroughly explained. Chapter 4 delineates the results of all analyzes. Finally, Chapter 5 summarizes the findings and observations of this study.

doi:10.6342/NTU202402878

Chapter 2 Dataset

In this study, we collected the experimental results from the PEER structural performance database [50], as well as previous researchs undertaken at the National Center for Research on Earthquake Engineering (NCREE) [4][5][51]. Figure 2.1 presents the implementation years for all the experiments in the PEER and NCREE database. These experiments were conducted in accordance with the prevailing bridge design specifications of their respective periods. Over time, these specifications undergo revisions and advancements. For instance, American Association of State Highway and Transportation Officials (AASHTO) published the Standard Specifications for Highway Bridges. Between 1931 and 1970, the design approach incorporated within these standard specifications was the Allowable Stress Design (ASD) methodology. Since 1970, to more accurately account for the variability in load considerations, the Load Factor Design (LFD) methodology was introduced. In 1994, the first edition of Load and Resistance Factor Design (LRFD) Bridge Construction Specifications [52] were published. However, from 1970 to 2007, the ASD and LFD specifications have coexisted. After 2007, all new bridges should be designed to follow the LRFD criteria. As of now, these specifications continue to be updated and revised to refine design methodologies aimed at enhancing the seismic performance of bridge columns. The assembled dataset encompasses a range of temporal editions and variants of bridge design specifications. This diversity enables our model to adapt and

doi:10.6342/NTU202402878

proficiently address a wide range of design types.

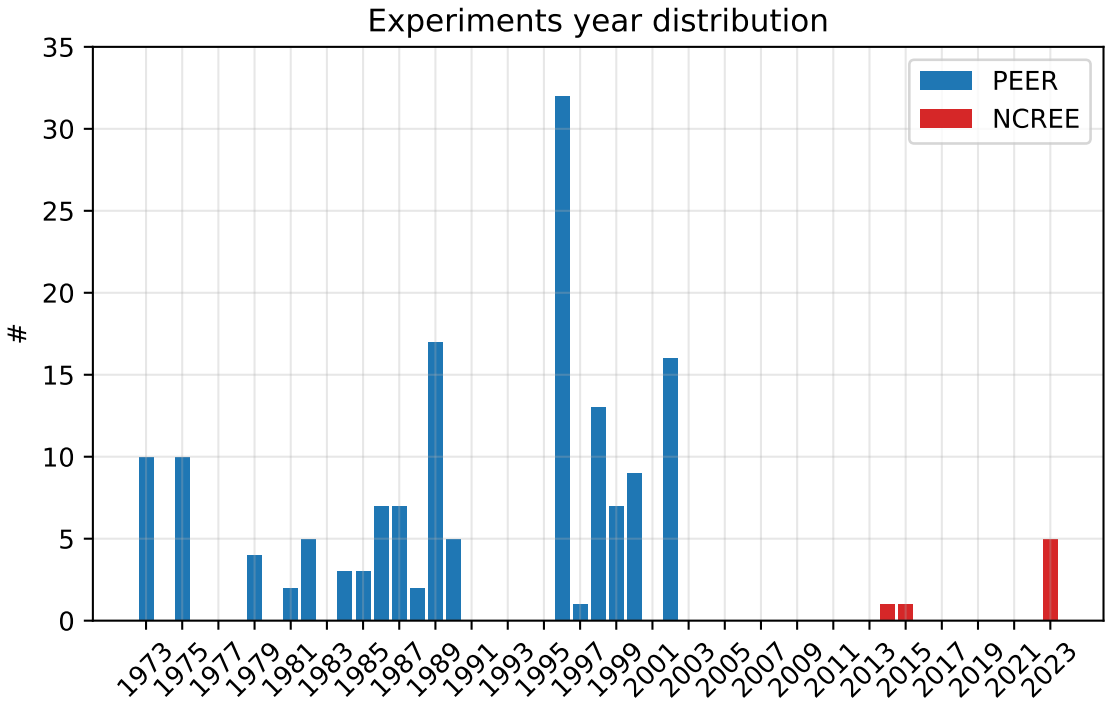

Figure 2.1: Distribution of implementation years from the PEER and NCREE databases. It is evident that the experiments documented within the PEER database span the years from 1973 to 2003. In contrast, the specimens cataloged in the NCREE database comply to contemporary design specifications after 2014.

Following the results collected from the experiments, two databases are investigated, the hysteresis database and the damage pattern database. The hysteresis database comprises the column design configurations and the hysteretic response data obtained through quasi-static experiments sourced from the PEER structural performance database, as well as NCREE database. On the other hand, due to the unavailability of damage pattern data within the PEER database, the damage pattern database is exclusively derived from the experimental results obtained at NCREE. The details of the hysteresis database and the damage pattern database are introduced in Sections 2.1 and 2.2, respectively.

doi:10.6342/NTU202402878

2.1 Hysteresis Database

The hysteresis database contains 160 hysteresis loops, including 153 from the PEER structural performance database and 7 from cyclic loading experiments carried out at NCREE. All specimens in the database are rectangular reinforced columns. The database includes the hysteretic responses observed during cyclic loading tests on reinforced concrete columns, along with details of the column design, such as geometry, material properties, loading, and reinforcement details.

2.1.1 Column Features

Figure 2.2 presents the complex considerations in column design. The design parameters gathered are categorically divided into four principal domains: material, geometry, loading, and reinforcement configuration. Within the category of material properties, the collected parameters include the maximum strength of unconfined concrete, the yield stress, and the maximum strength of longitudinal and transverse reinforcement steels. These material properties are determined through material testing methods, such as concrete cylinder compression test and rebar tensile test. However, the behavior of confined concrete introduces additional complexity that cannot be fully captured through standard material experiments. To address this, we adopt theoretical models such as the Mander confined concrete model [53], which offers a robust framework to understand the stress-strain relationship in confined concrete scenarios. A detailed description of the Mander confined concrete model will be provided in Section 2.1.2. Proceeding to the geometric parameters, we define the critical dimensions, including section width, section depth, and column height. These dimensions govern not only the spatial configuration of the col-

doi:10.6342/NTU202402878

umn, but also significantly affect its load-carrying capacity. By thoroughly configuring the reinforcement setup, the longitudinal rebars can be precisely positioned at the designated locations. In the evaluation of transverse reinforcement, stirrups or ties provide confinement to the core concrete. The confinement effects are integrated using the Mander model.

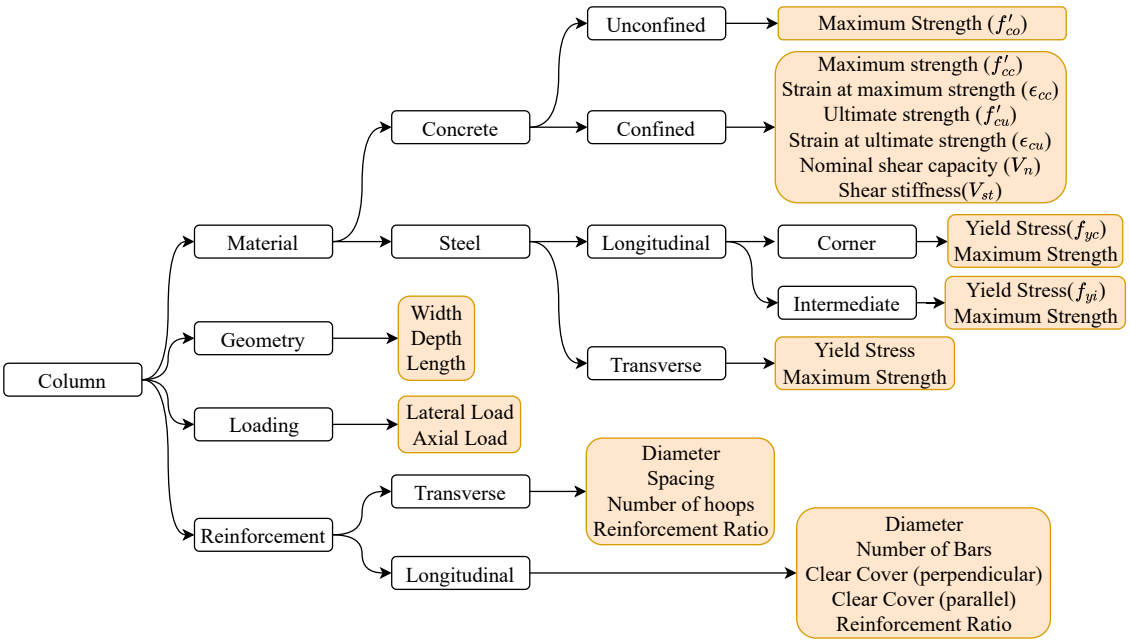

Figure 2.2: The collected column features from original document for all column specimens in hysteresis database.

2.1.2 Mander Confined Concrete Model

The Mander confined concrete model, as proposed by [53], is formulated to predict the stress-strain response of confined concrete, characterized by concrete encased with transverse reinforcements such as steel hoops or ties. Mander et al. suggested the arching mechanism that occurs between discrete levels of rectangular hoop reinforcement. At the midpoint between transverse reinforcement levels, the extent of insufficiently confined concrete reaches its maximum, while the core area of effectively confined concrete area is the smallest. For rectangular columns, the arching mechanism is modeled as taking

doi:10.6342/NTU202402878

the form of second-degree parabolas, initiating with a tangent slope of 45 °. This arching mechanism emerges vertically between layers of transverse hoop bars and horizontally between longitudinal reinforcement bars, which can be observed in Figure 2.3.

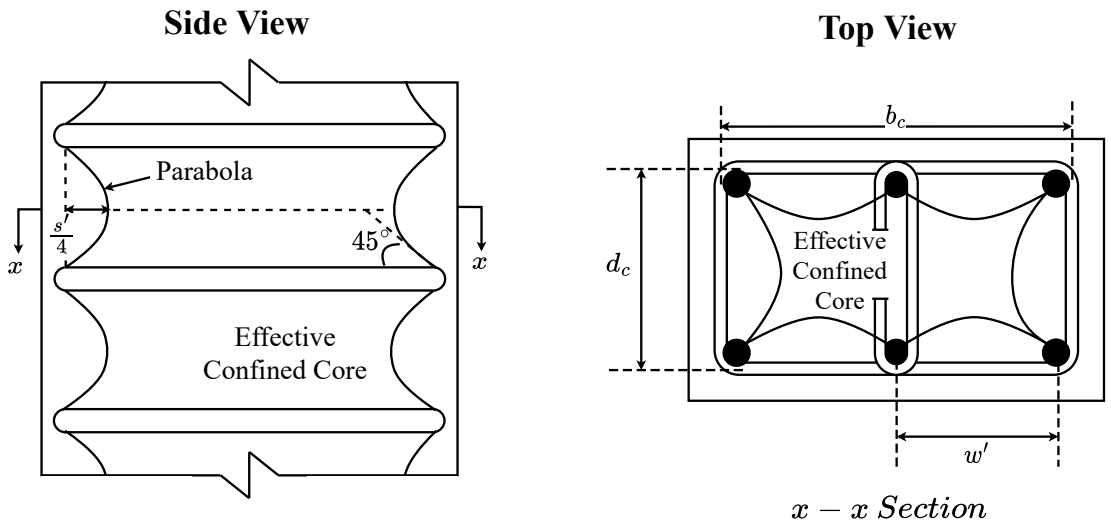

Figure 2.3: Arching mechanism assumed by the Mander confined concrete model.

The stress-strain relationship described by the Mander confined concrete model is presented in Figure 2.4 and can be calculated by the following formulas:

$$f_c = \frac{f'_{cc} x r}{r - 1 + x^r} \tag{2.1}$$

with

$$x = \frac{\epsilon_c}{\epsilon_{cc}} \tag{2.2}$$

$$\epsilon_{cc} = \epsilon_{co}[1 + 5(\frac{f'_{cc}}{f'_{co}} - 1)] \tag{2.3}$$

$$r = \frac{E_c}{E_c - E_{sec}} \tag{2.4}$$

$$E_c = 5000\sqrt{f_{co}} \tag{2.5}$$

$$E_{sec} = \frac{f'_{cc}}{\epsilon_{cc}} \tag{2.6}$$

doi:10.6342/NTU202402878

where f_c is the longitudinal stress in concrete; ϵ_c is the longitudinal strain in concrete; f'_{cc} is the maximum stress of confined concrete; ϵ_{cc} is the strain at f'_{cc}; E_c and E_{sec} is the modulus of elasticity of the unconfined concrete and confined concrete.

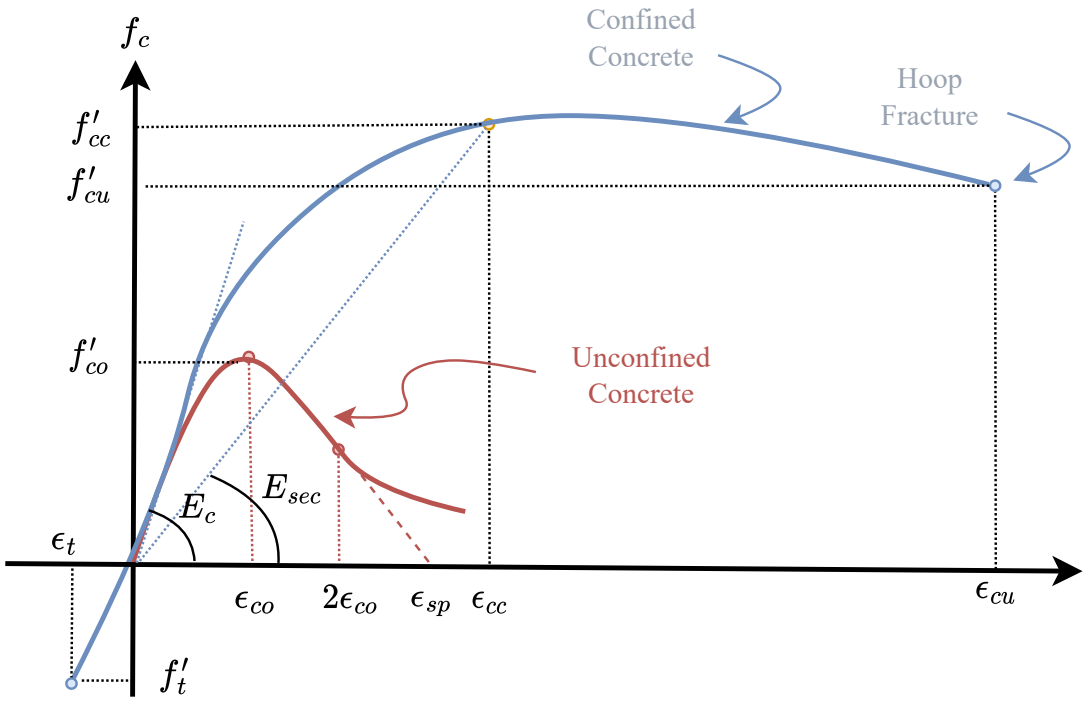

Figure 2.4: The sress-strain relationship defined by the Mander confined concrete model.

From the equations above, the values of f'_{cc} is needed to construct all the strain-stress relationship. However, determining f'_{cc} is complex and requires an iterative procedure. In this study, we followed the proposed approximate equation from Chang and Mander [54], that can be utilized to determine the value of f'_{cc}. The f'_{cc} can be calculated with the following equations:

$$f'_{cc} = f'_{co}[1 + A\bar{x}(0.1 + \frac{0.9}{1 + B\bar{x}})] \tag{2.7}$$

with

$$\bar{x} = \frac{f'_{lx} + f'_{ly}}{2f'_{co}} \tag{2.8}$$

$$R = \frac{f'_{lx}}{f'_{ly}} \quad f'_{lx} \geq f'_{ly} \tag{2.9}$$

doi:10.6342/NTU202402878

$$A = 6.88886 - (0.6069 + 17.275R)e^{-4.989R} \tag{2.10}$$

$$B = \frac{4.5}{\frac{5}{A}(0.9849 - 0.6306e^{-3.8939R}) - 0.1} - 5 \tag{2.11}$$

where f'_{lx} and f'_{ly} are the effective confining lateral stress from the transverse reinforcement with x and y direction. The effective confining lateral stress can be defined by the following equation:

$$f'_{lx} = \frac{1}{2}k_e\rho_{sx}f_{yh} \tag{2.12}$$

$$f'_{ly} = \frac{1}{2}k_e\rho_{sy}f_{yh} \tag{2.13}$$

where ρ_{sx} and ρ_{sy} are the ratios of the volume of transverse confining steel to the volume of confined concrete core along x and y direction, respectively; f_{yh} is the yield strength of the transverse reinforcement; k_e is the confinement effectiveness coefficient defined as the ratio between volumns from effective core and confined concrete ($\frac{A_e}{A_{cc}}$).

Following the Equation 2.7, the value of f'_{cc} can be determined. After that, the ultimate condition should be defined. As suggested by Lehman [55], the ultimate strain ϵ_{cu} when the first hoop fractures can be calculated using the following equation:

$$\epsilon_{cu} = 0.004 + \frac{\rho_s f_{yh}\epsilon_{su}}{f'_{co}} \tag{2.14}$$

where ρ_s and f_{yh} are the volumetric ratio of the transverse reinforcement and the yield strength, respectively. ϵ_{su}, assumed to be 0.14 in this study, is the fracture strain of transverse steel. Subsequent to determining ϵ_{cu}, the value of f'_{cu} can be derived using Equation 2.1. The nominal shear capacity of the columns is also calculated based on the Caltrans Seismic Design Criteria (SDC) [56] during the collection of column information.

doi:10.6342/NTU202402878

2.1.3 Failure Types and Hysteresis Loop

Typically, bridge failures can be categorized into three distinct types, namely, flexural, flexural-shear, and shear failures. Among the various failure modes, the shape and deterioration of hysteresis loops exhibit notable differences. Figure 2.5 presents the hysteresis loops sampled from the hysteresis database with three different failure types. In bridge columns, flexural failure is typically characterized by yielding of the reinforcement followed by crushing of the compression concrete. It is considered a ductile failure mode because it allows for large deformations before collapse, providing sufficient warning before failure. The hysteresis loops in this case display wide loops with significant energy dissipation. Shear failure is a fragile failure mode that happens when the transverse forces exceed the shear strength of the column. It results in a sudden loss of strength and stiffness, often without significant prior deformation, making it a dangerous failure mode as it provides little warning before collapse. The hysteresis loops for shear failure are typically narrow with a steep drop-off after the peak load, indicating limited energy dissipation and ductility. The flexural-shear failure mode combines the characteristics of flexural and shear failures. Figure 2.5 dipicts the hysteresis loops for different failure types from the data in the hystersis database. The PEER database comprises 153 RC column specimens, of which 116 indicate flexural failure, 22 indicate flexural-shear failure, and 15 indicate shear failure. On the other hand, all seven specimens in the NCREE database indicate flexural failure.

doi:10.6342/NTU202402878

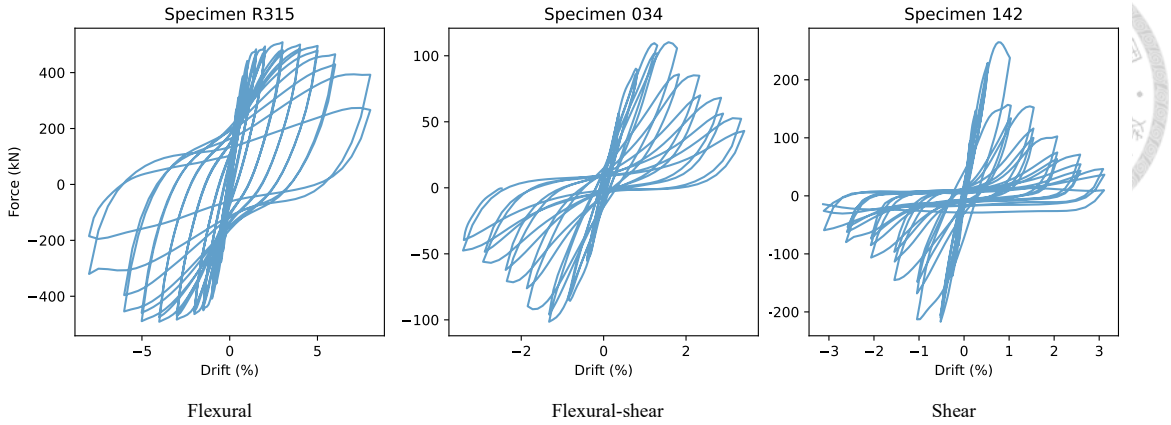

Figure 2.5: Hysteresis loops for different failure types.

2.2 Damage Pattern Database

The damage pattern database contains data pairs with a damage pattern, time step in the hysteresis loop, and the corresponding performance level, i.e., Damage Index (DI). As the damage patterns are not accessible in the PEER performance database, the available damage patterns are exclusively derived from the column specimens R307, R315, R330, R615, R1015, and CTR1 conducted at NCREE.

2.2.1 Damage Indicator

This study adopts the damage model proposed by Park and Ang [48] to assess seismic structural damage. Park and Ang quantified the DI based on the principle that seismic damage to structural elements is induced by the interactive effect of the peak structural deformation and cumulative energy dissipation incurred through successive seismic excitation. The formula for calculating the DI is given below:

$$\mathrm{DI} = \frac{\delta_m}{\delta_u} + \lambda \frac{\int dE}{F_y \delta_u} \tag{2.15}$$

doi:10.6342/NTU202402878

where δ_m denotes the peak displacement experienced by a column under cyclic or seismic excitation; δ_u signifies the ultimate displacement of a column subjected to monotonic loading; $\int dE$ represents the cumulative hysteretic energy dissipation; F_y denotes the yield force, and λ is a parameter utilized to correlate hysteretic energy dissipation.

Table 2.1 presents the strength deterioration parameters, specifically δ_u, λ, and F_y, for six specimens documented within the NCREE database. Based on the analysis conducted by Wang et al. [4], the parameter δ_u was derived utilizing empirical methods for determining the plastic hinge length and the ultimate compressive deformation of confined concrete, as formulated by Priestley et al. [57]. Subsequently, the value of λ was determined based on the experimental hysteresis loop at a state of 20% strength degradation in order to obtain δ_m and $\int dE$ in Equation 2.15, with DI set to one. The DI can be evaluated based on the calibrated strength deterioration parameters presented in Table 2.1. The corresponding DI can be calculated using equation 2.15, using δ_m and $\int dE$ obtained from the respective time step.

Table 2.1: Calibrated strength deterioration parameters for each column specimen in the damage pattern database.

Experiments	Damage Model Parameters		
	δ_u (mm)	F_y (KN)	λ
R307	161	368	0.140
R315	136	508	0.057
R330	107	808	0.025
R615	356	256	0.066
R1015	822	160	0.140
CTR1	234	921	0.101

2.2.2 Damage Patterns and Image Preprocessing

During the cyclic loading tests, the photos were automatically taken from two different angles when the drift ratio reached the reversal points. Reversal points indicate the

doi:10.6342/NTU202402878

moments at which the direction of the applied force is inverted, denoting that the drift ratio has reached its peak value within the respective cycle. Afterward, following the data preprocessing techniques from our previous work [47], a homography transformation is applied to achieve orthographic projection on the two weak surfaces of the RC columns. Homography constitutes a transformation that describes the correspondence of points between two planes. These planes are generally correlated with distinct perspectives or views of an identical scene. The planar homography describes the transformation between two planes, which can be mathematically represented by the following equation:

$$s \begin{bmatrix} x' \\ y' \\ 1 \end{bmatrix} = \mathbf{H} \begin{bmatrix} x \\ y \\ 1 \end{bmatrix} = \begin{bmatrix} h_{11} & h_{12} & h_{13} \\ h_{21} & h_{22} & h_{23} \\ h_{31} & h_{32} & h_{33} \end{bmatrix} \begin{bmatrix} x \\ y \\ 1 \end{bmatrix} \tag{2.16}$$

The homography matrix, denoted as **H**, constitutes a matrix 3×3 having 8 degrees of freedom, attributed to its estimation only up to a scalar multiple. To accurately compute **H**, at least four pairs of corresponding points between the two planes are required. This requirement results from the need to solve a system of linear equations that arises from point correspondences, which ultimately yields the elements of the homography matrix. This process converts the surface of the columns from an isometric view to an orthographic view and removes the complex background, allowing a detailed examination of the damage patterns on the surface. During the cyclic loading experiments, $100\text{mm} \times 100\text{mm}$ grids were marked on the column surfaces to facilitate the evaluation of the spalling area. Consequently, a standardized area measuring 750mm $\times$ 800mm is designated for all specimens to regulate the region of interest. This standardization facilitates the precise quantification of the spalling height and area. The homography between two planes and the transformed

doi:10.6342/NTU202402878

damage pattern are presented in Figure 2.6.

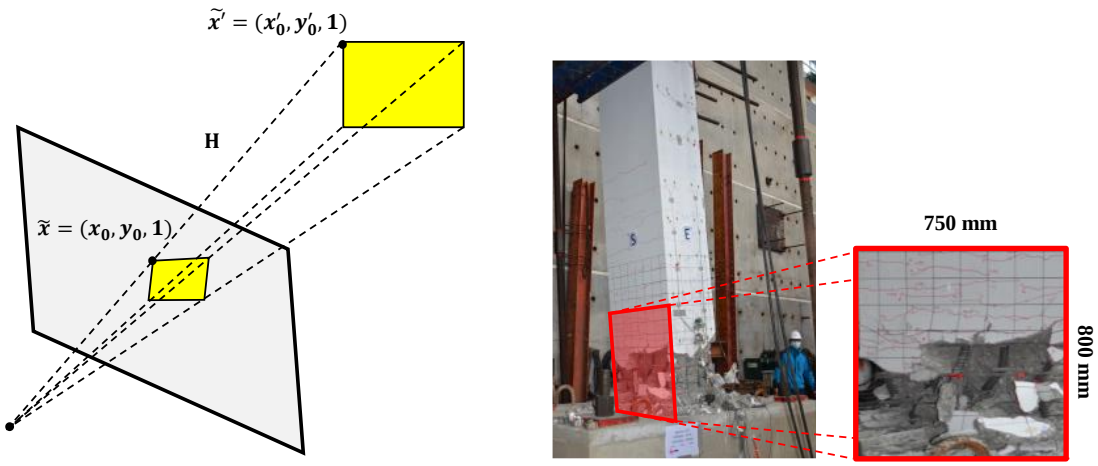

Figure 2.6: Homography relationship between two planes and the transformed damage patterns.

To facilitate training and validation of both the HysGAN and the DI prediction network, the data are random selected in an 85:15 ratio from the five specimens, namely, R307, R315, R330, R615, and R1015. The damage patterns from the CTR1 specimen are used as a test dataset to evaluate the generalizability. Table 2.2 presents the numbers of the collected damage patterns in different datasets. In Figure 2.7, two pairs of samples from the damage pattern database are shown.

Table 2.2: Numbers of collected damage patterns with training, validation, and test data.

Type	R307	R315	R330	R615	R1015	CTR1
Train	108	112	103	118	116	-
Validation	20	20	20	22	22	-
Test	-	-	-	-	-	124

doi:10.6342/NTU202402878

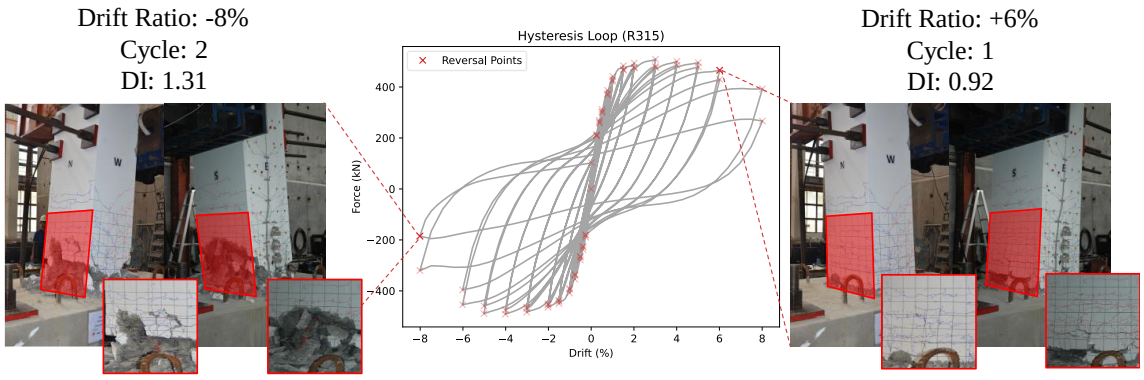

Figure 2.7: Data pairs of R315 sourced from the damage pattern database exhibiting drift ratio +6% (first cycle) and -8% (second cycle).

doi:10.6342/NTU202402878

Chapter 3 Methodology

In this section, the prognostic framework for forecasting bridge damage patterns and predicting hysteretic behavior is introduced. The comprehensive procedure and experiment for the entire framework is shown in Figure 3.1.

First, we propose an automatics simulation method using OpenSeesPy library [58] based on OpenSees framework [59] to construct the finite element model. By considering the column design and the loading protocol, the simulated response can be obtained. The simulation process is introduced in Section 3.1. Subsequently, to predict the hysteretic response of the bridge column, we develop a sequence-to-sequence hysteresis prediction network, referred to as HysGRU. Conceptually, we endeavor to predict the hysteresis loop directly from column design parameters and loading protocols. Nevertheless, the complexity of hysteretic behavior implies that a purely data-driven approach may yield inferior performance. Therefore, we integrate simulation results to guide HysGRU, facilitating improved predictive accuracy. The details are described in Section 3.2.

In Section 3.3, the proposed damage patterns generative model, HysGAN, is presented. HysGAN is developed on the basis of CGAN, allowing to synthesize high-fidelity damage patterns according to the given condition. Regarding the conditional input type, HysGAN is first controlled based on column characteristics and Damage Index (DI). Nev-

doi:10.6342/NTU202402878

ertheless, the computation of DI necessitates a thorough analytical process, with experimental validation required to determine its feasibility. As a result, we endeavor to incorporate the latent features extracted from hysteresis loop by the HysGRU, allowing us to generate the corresponding damage patterns for each drift ratio. To effectly evaluate the generative performance of HysGAN, a DI prediction network and a spalling segmentation method are proposed to quantify the damage, since the damage mechanisms affecting RC bridge columns are extremely complex. Trained from the authentic data, we can evaluate the performance of HysGAN by assessing the accuracy from the prediction of synthetic data. Furthermore, we proposed a computer vision-based segmentation methodology to estimate the height and area of concrete spalling, thereby facilitating the evaluation of the generalizability of HysGAN. The comprehensive introduction is described in Section 3.4.

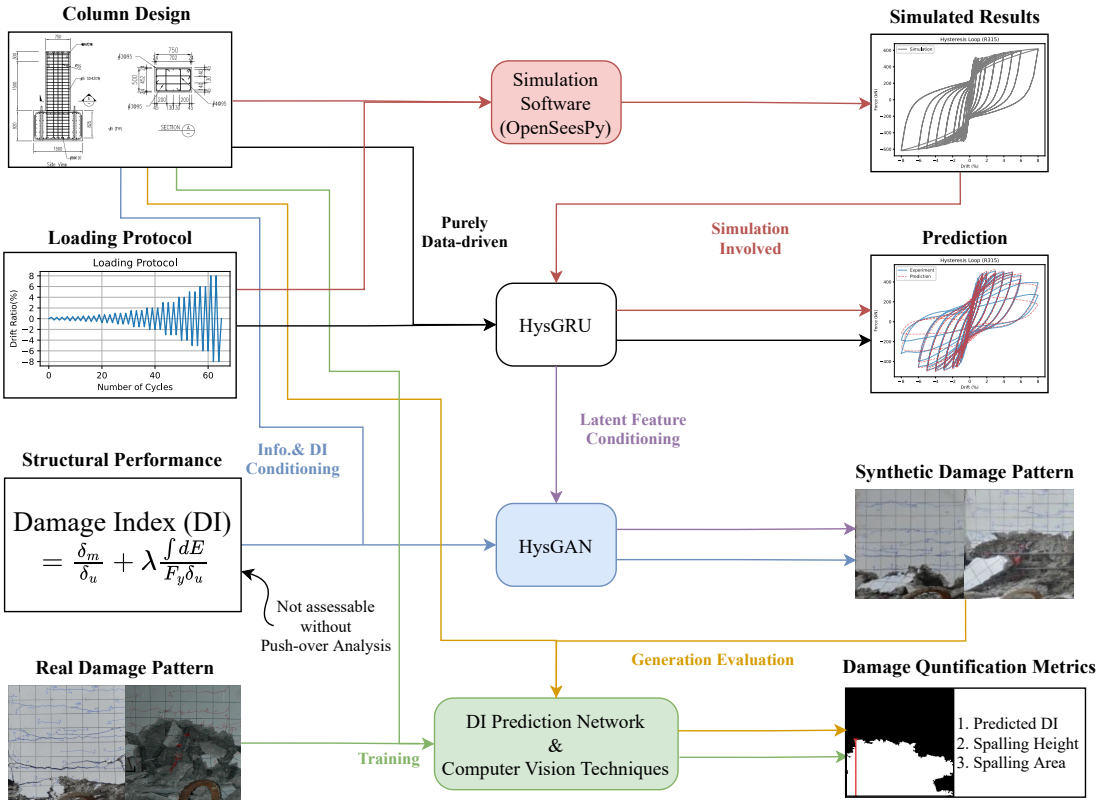

Figure 3.1: The proposed prognostic framework for bridge failure forecasting, hysteretic behavior prediction, and damage quantification.

doi:10.6342/NTU202402878

3.1 Finite Element Simulation

OpenSeesPy, an open source Python module designed for OpenSees, a finite element framework, is used to construct the numerical model. We proposed a simulation process that can estimate the simulated hysteretic behavior of the RC bridge columns. First, Concrete02 and Steel02 models are utilized to depict the uni-axial behavior of concrete and steel, respectively. The stress-strain relationships for both models are presented in Figure 3.2. The input parameters of the constitutive models of unconfined concrete, confined concrete, and longitudinal rebars can be determined by the information collected from the hysteresis database. Table 3.1 presents the setting for the consecutive model of the materials.

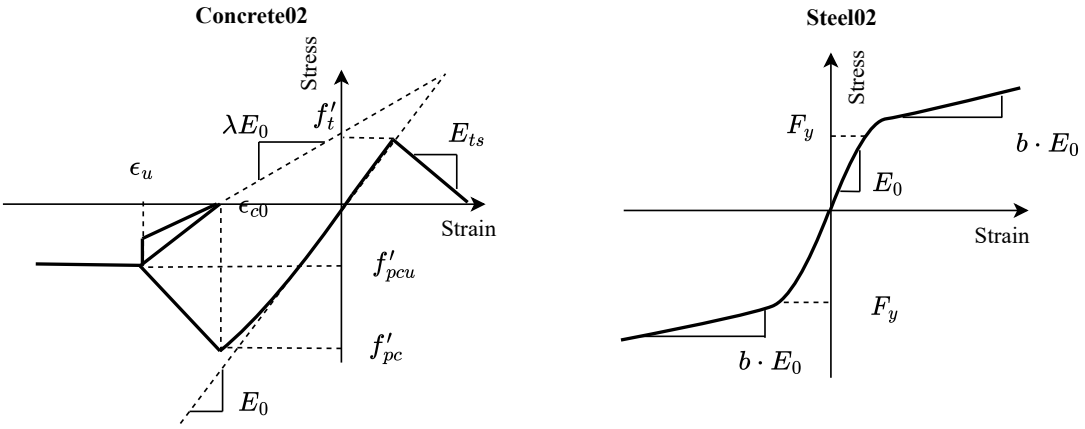

Figure 3.2: The constitutive material model described by Concrete02 and Steel02.

After the setup of material properties, the finite element model is constructed using four displacement-based beam-column element objects, and the deformations are solved with Gaussian-Lobatto integration points. Each integration point has the same fiber section. Based on the actual section configuration derived from the hysteresis database, the uni-axial material constitutive models are allocated to the corresponding location to define the axial and flexural behavior of the fiber section through discretization. In addition, the

doi:10.6342/NTU202402878

shear force-deformation relationship is defined for each section with the nominal shear capacity (V_n) and the shear stiffness (V_{st}).

Table 3.1: The prescribed parameters for the uni-axial sequential material models applicable to (a) concrete, and (b) steel. (f'_{co}: Maximum strength of unconfined concrete; f'_{cc}: Maximum strength of confined concrete; ϵ_{cc}: Corresponding strain at f'_{cc}; f'_{cu}: Ultimate strength of confined concrete at the point of transverse steel fracture; E_c: The modulus of elasticity derived from the expression $12000\sqrt{f'_{cc}}$).

(a) Concrete.

Concrete	f'_{pc}(kN)	ϵ_{c0}	f_{pcu}(kN)	ϵ_u	λ	f_t(kN)	E_{ts}(MPa)
Unconfined	f'_{co}	0.002	0.0	0.005	0.1	-0.04f'_{co}	0.02E_c
Confined	f'_{cc}	ϵ_{cc}	f'_{cu}	ϵ_{cu}	0.1	-0.04f'_{cc}	0.02E_c

(b) Steel.

Steel	F_y(kN)	E_0(MPa)	b	cR_0	$cR1$	$cR2$
Corner	f_{ys}	210000	0.025	18.0	0.925	0.15
Intermediate	f_{yi}	210000	0.025	18.0	0.925	0.15

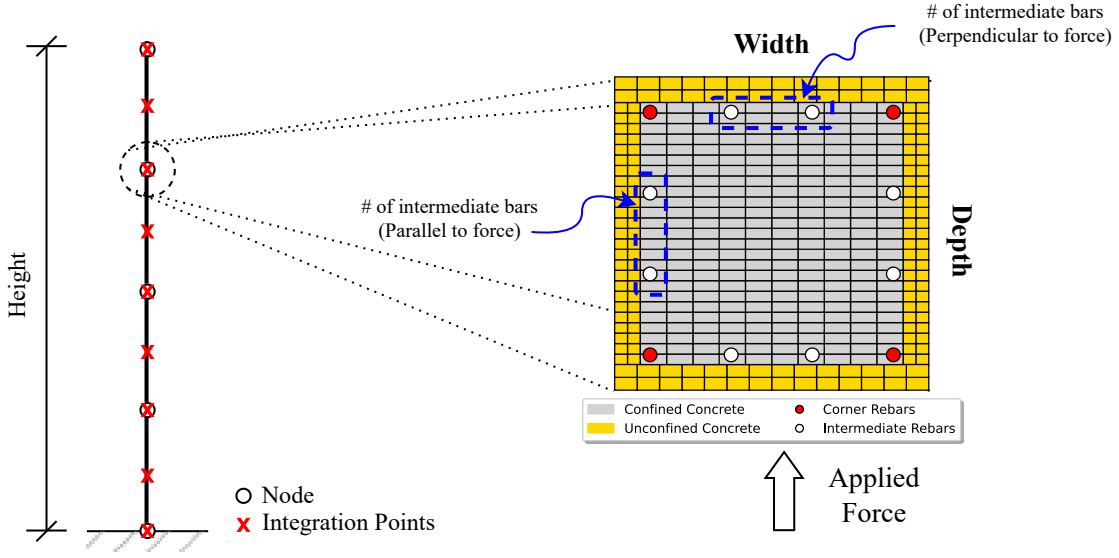

Figure 3.3: Schematic view and fiber section setting of the nonlinear model constructed using OpenSeespy.

3.2 Hysteresis Prediction Network

In prior investigations, there exists a notable deficiency in directly addressing the sequential prediction of hysteretic behavior in bridge columns within the domain of deep learning research. As a result, we address this issue with the network based on Recurrent

doi:10.6342/NTU202402878

Neural Networks (RNNs). However, traditional RNNs often struggle with long-term dependencies due to issues such as vanishing gradients. Gated Recurrent Units (GRUs) [60] effectively address these challenges through the implementation of gating mechanisms that control the transmission of information within the network. The calculation process of one GRU cell is dipicted in Figure 3.4a. By iteratively computing along the time series, the hidden state for each time step can be extracted. In order to capture context and dependencies in the data from different direction, a bidirectional architecture has been employed to process input sequences in both forward and backward directions simultaneously. The structure of the bidirectional GRU (biGRU) is shown in Figure 3.4b.

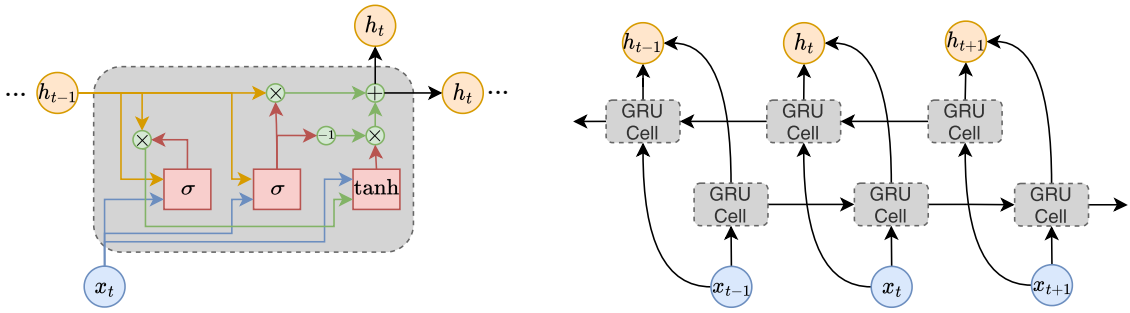

(a) (b)

Figure 3.4: Structure of (a) GRU cell and (b) Bidirectional GRU (BiGRU).

Renowned for the superior efficiency and capability to model dependencies over extended sequences, GRUs have emerged as a preferred methodology in numerous applications necessitating the processing of sequential data. As a result, we propose a GRU-based network for hysteresis loop predictions, namely HysGRU. The detailed architecture of the HysGRU is illustrated in Figure 3.5. Following the evolution of the GRU, we develop an RNN extractor based on GRU to extract latent features within hysteresis loops, which is denoted by $\mathbf{h}$. Subsequently, a multilayer perceptron (MLP) predictor is employed to estimate the corresponding force for each drift ratio based on the input data, denoted by $\hat{\mathbf{F}}$. The input for this task encompasses 17 distinct column features, a singular drift ratio,

doi:10.6342/NTU202402878

and an associated force, derived from simulation at each incremental stage of the discrete drift ratio. For model convergence facilitation, the column features were preprocessed via standardization using their respective means and standard deviations. The length of each hysteresis loop is symbolized by L; hence, the input dimensions can be expressed as $L \times 19$. Furthermore, to assess performance within a purely data-driven framework, the associated simulated force is excluded, thereby yielding input dimensions of $L \times 18$. Due to the iterative computation inherent in the GRU network, it is capable of handling hysteresis loops of varying lengths. Regarding the hyperparameters, the hidden dimension, represented as $Hidden\ Dim.$, and the number of layers, delineated as n, are set as 512 and 4, respectively. Furthermore, a bidirectional architecture has been employed to process input sequences in both forward and backward directions simultaneously, enhancing its ability to capture context and dependencies in the data. The extracted hidden states from the forward and backward directions will be concatenated. Consequently, the dimension of the output from the RNN extractor is given by $L \times (Hidden\ Dim. \times 2)$. Ultimately, the MLP predictor performs a linear transformation on the terminal dimension of the latent features, enabling the prediction of the corresponding force with a dimension of $L \times 1$ without modifications to the model weights in relation to the length of the hysteresis loop.

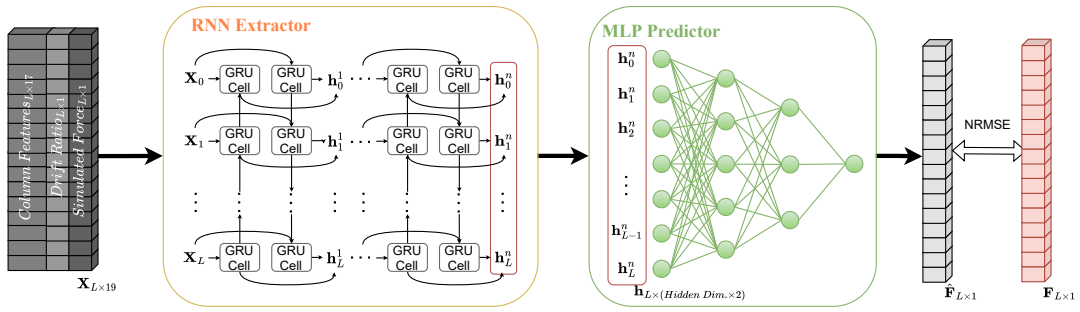

Figure 3.5: Detailed structure of HysGRU.

In this task, the normalized root mean squared error (NRMSE) is utilized as the loss function to iteratively refine the network parameters. The NRMSE standardizes the error

doi:10.6342/NTU202402878

by the range of values, defined by the difference between the maximum and minimum values. It provides a scale-independent measure of prediction accuracy, allowing comparisons across different hysteresis loops without being affected by the scale of the data. The NRMSE is expressed as follows:

$$Root\ mean\ squared\ error\ (RMSE) = \sqrt{\frac{1}{L}\sum_{i=1}^{L}(\hat{\mathbf{F}}_i - \mathbf{F}_i)^2} \tag{3.1a}$$

$$Normalized\ root\ mean\ squared\ error\ (NRMSE) = \frac{RMSE}{\mathbf{F}_{max} - \mathbf{F}_{min}} \tag{3.1b}$$

For the configuration of this training task, the Adam optimization algorithm [61] is utilized. The parameters β_1 and β_2 are fixed at 0.9 and 0.999, respectively, to optimize the network parameters. The initial learning rate is set to 5e-6, incorporating a warmup phase of 500 epochs, and gradually increasing to a peak value of 1e-4, subsequently employing a cosine annealing schedule. The total number of training epochs is 5000.

3.3 Damage Pattern Generation Network

To prognosticate the damage pattern, a CGAN-based generative model is introduced, namely HysGAN. The conventional GAN [42] architecture consists of two neural networks, i.e. the generator and the discriminator. The objective of the generator is to deceive the discriminator by generating high-quality images. On the other hand, the discriminator acts as a critic that evaluates the authenticity of the generated images. Through adversarial training, these networks engage in a competitive process, ultimately yielding high-fidelity generated images. However, since the generator only utilizes stochastic noise as input, it limits our ability to control the generation of the desired synthetic images. A CGAN ex-

doi:10.6342/NTU202402878

tends the GAN framework by introducing additional conditions to both the generator and the discriminator, allowing CGAN to generate the output conditioned on specific input variables.

In this task, we endeavor to leverage the information from the hysteresis loop. Intuitively, we can analyze the hysteresis loop predicted from the previous task to assess the Damage Index (DI) under different drift ratio. However, the determination of δ_u from Equation 2.15 requires the execution of a monotonic push-over analysis, which requires experimental data to evaluate the accuracy of the simulated results. Consequently, HysGAN aims to produce the corresponding damage patterns by modulating latent features as a conditional input to the generator. Figure 3.6 illustrates the architecture of the proposed HysGAN. To acquire the informative latent features from the hysteresis loop, we employ the pre-trained HysGRU to extract the latent features corresponding to each drift ratio under different conditions. The HysGRU was initially trained utilizing the hysteresis database, and its weight parameters are subsequently fixed for this task. These latent features are subsequently utilized as conditional inputs to modulate the synthetic images produced by the generator. For instance, to generate the damage pattern associated with the drift ratio at time step $L-1$, one can utilize $\mathbf{h}_{L-1}^{n}$ as the conditional input to generate the corresponding damage pattern. Consequently, the input condition for the generator comprises random noise, latent features, and the orientation of the weak surface.

For the loss functions, we discuss the impacts of three adversarial generative loss functions to experiment the efficacy of the proposed generative models, that is, the loss of Standard GAN (SGAN), Relative Standard GAN (RSGAN), and Relative average Standard GAN (RaSGAN) loss [62]. In SGAN, the discriminator is trained to differentiate between authentic and synthetic images by estimating the probability that a given input is

doi:10.6342/NTU202402878

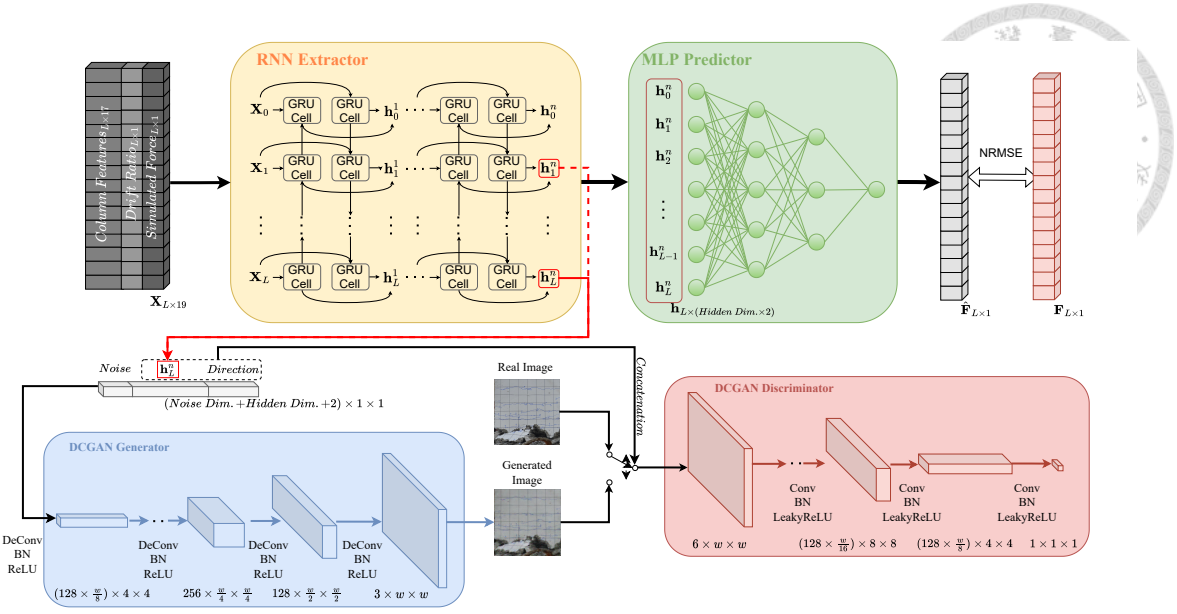

Figure 3.6: The network architecture for proposed HysGAN.

real. The generator endeavors to create synthetic images that the discriminator will recognize as authentic. The corresponding loss functions are formulated by the following equations:

$$\begin{cases} L_D^{SGAN} = -\mathbb{E}_{x_r \sim \mathbb{P}}\Big[log\Big(\sigma\big(D(x_r|c)\big)\Big)\Big] - \mathbb{E}_{x_f \sim \mathbb{Q}}\Big[log\Big(1-\sigma\big(D(x_f|c)\big)\Big)\Big] \\ L_G^{SGAN} = -\mathbb{E}_{x_f \sim \mathbb{Q}}\Big[log\Big(\sigma\big(D(x_f|c)\big)\Big)\Big] \end{cases} \tag{3.2}$$

where x_f is the synthetic image; x_r is the authentic image; c is the condition input of the generator; $D(x)$ is the discriminator evaluated at x; $\sigma(x)$ is the sigmoid function; $\mathbb{P}$ and $\mathbb{Q}$ are the distributions of the real and fake images, respectively.

However, SGAN loss often faces stability issues and may produce poor-quality outputs, particularly in scenarios where the discriminator is able to precisely differentiate between authentic and synthetic data. Consequently, RSGAN loss modifies the standard approach by introducing a relativistic discriminator. Instead of assessing the absolute

doi:10.6342/NTU202402878

probability that a given image is real, the relativistic discriminator estimates the likelihood that a real image is more realistic than a randomly sampled fake image. The formulation of the loss functions is provided in Equation 3.3. This relative comparison encourages the generator to create fake data that not only looks real but also outperforms real data in terms of realism, leading to more stable training and higher quality output.

$$\begin{cases} L_D^{RSGAN} = -\mathbb{E}_{(x_r,x_f)\sim(\mathbb{P},\mathbb{Q})}\Big[log\Big(\sigma\big(D(x_r|c) - D(x_f|c)\big)\Big)\Big] \\ L_G^{RSGAN} = -\mathbb{E}_{(x_r,x_f)\sim(\mathbb{P},\mathbb{Q})}\Big[log\Big(\sigma\big(D(x_f|c) - D(x_r|c)\big)\Big)\Big] \end{cases} \tag{3.3}$$

Furthermore, RaSGAN loss extends the relativistic approach by considering the average realism of real and fake data. The discriminator estimates the probability that a real data point is more realistic than the average of fake data, and vice versa. The derivation of the loss functions is defined in Equation 3.4.

$$\begin{cases} L_D^{RaSGAN} = -\mathbb{E}_{x_r\sim\mathbb{P}}\Big[log\big(\tilde{D}(x_r|c)\big)\Big] - \mathbb{E}_{x_f\sim\mathbb{Q}}\Big[log\big(1-\tilde{D}(x_f|c)\big)\Big] \\ L_G^{RaSGAN} = -\mathbb{E}_{x_f\sim\mathbb{Q}}\Big[log\big(\tilde{D}(x_f|c)\big)\Big] - \mathbb{E}_{x_r\sim\mathbb{P}}\Big[log\big(1-\tilde{D}(x_r|c)\big)\Big] \end{cases} \tag{3.4}$$

where $\tilde{D}(x_r|c) = \sigma\big(D(x_r|c) - \mathbb{E}_{x_r\sim\mathbb{P}}D(x_r|c)\big)$; $\tilde{D}(x_f|c) = \sigma\big(D(x_f|c) - \mathbb{E}_{x_f\sim\mathbb{Q}}D(x_f|c)\big)$.

In configuring this training task, the Adam optimization algorithm is employed, with the hyperparameters β_1 and β_2 set to 0.9 and 0.999, respectively. During each epoch, the update procedure involves sequentially updating the discriminator and then the generator once. The learning rate is fixed at 1e-4, and the total number of training epochs is set to 3000.

doi:10.6342/NTU202402878

3.4 Damage Quantification

In order to quantify structural damage, one can assess the performance metrics of the structure or conduct an evaluation based on the visual damage observed on the structures. However, the evaluation of performance metrics typically demands extensive time investment and substantial background expertise. As a consequence, this study advocates for the implementation of a regression network to prognosticate performance metrics derived from visual damage assessments. Additionally, a computer vision-based methodology is introduced to approximately determine the height and area of concrete spalling. These methods are utilized to evaluate the consistency of synthetic damage patterns generated from HysGAN.

3.4.1 Damage Index Prediction

The Vision Transformer (ViT) [63] is a deep learning model architecture designed for image recognition tasks. ViT extends the utilization of the transformer architecture, initially conceived for natural language processing, to visual datasets. This model processes imagery by segmenting it into a sequence of fixed-size patches, each subject to linear embedding, augmented with positional encodings, and subsequently processed through a conventional transformer encoder. This approach allows ViT to capture long-range dependencies and complex patterns within images more effectively than traditional convolutional neural networks (CNNs). ViT has demonstrated competitive performance on image classification benchmarks, often outperforming CNNs. As a result, the proposed DI prediction network is constructed based on ViT to predict the DI by the visual damage pattern and the corresponding column features. Figure 3.7 depicts the comprehensive architecture

doi:10.6342/NTU202402878

of the proposed DI prediction network. The ViT extracts features from the image patches by utilizing the self-attention mechanism, subsequently concatenated with the features derived from the column design. Thereafter, the MLP predicts the value of DI.

In this task, we adhered to the partitioning schema of the damage pattern database, comprising 557 training images and 104 validation images. Furthermore, images sourced from CTR1 were employed as test data. For the training configuration, we utilized the pretrained ViT-Base Encoder with 16×16 patches trained from ImageNet [64] to fine-tune for our specific application. The MSE was adopted as the optimization criterion for the loss function. The Adam optimizer was employed with a fixed learning rate of 1e-6, and the model was subjected to 500 training epochs.

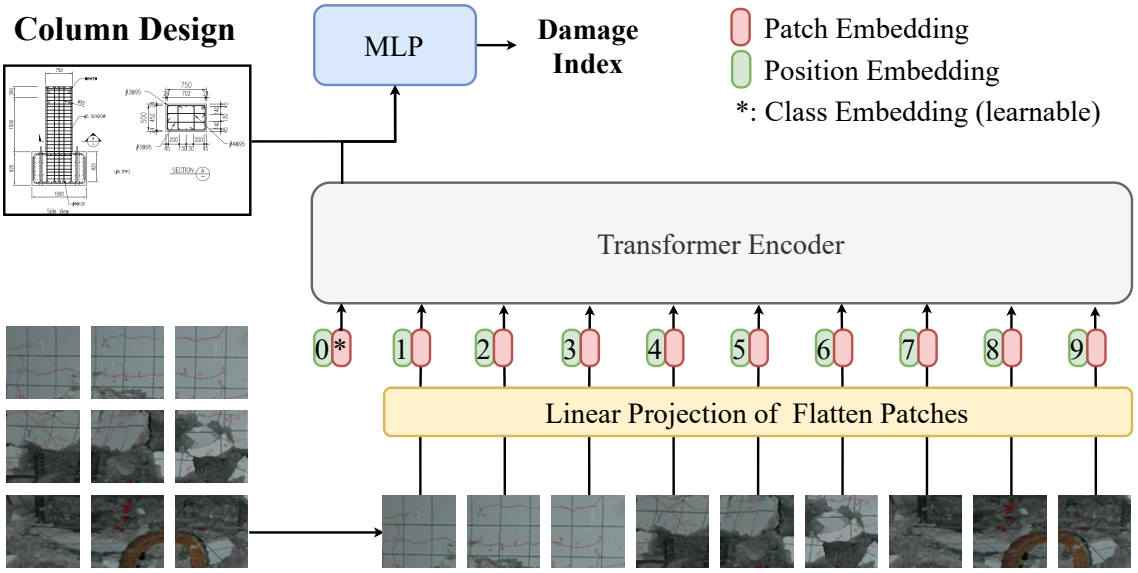

Figure 3.7: Proposed network for predicting the Damage Index (DI) from visual damage patterns and column design features.

3.4.2 Spalling Height and Area

In addition to the DI, the visual assessment of damage serves as a pivotal metric for evaluating structural integrity. We propose a method to segment the area and height of the

doi:10.6342/NTU202402878

concrete spalling region. The outlined procedure is illustrated in Figure 3.8. Initially, the K-nearest Neighbor (KNN) algorithm [65], is employed to cluster the pixel values. Following the application of homography transformation to project the damage pattern into an orthographic view, KNN effectively segments the concrete spalling area. Furthermore, morphological operations are utilized to mitigate noise, thereby improving the accuracy of the prediction. This allows for the determination of the spalling percentage and the height of the concrete spalling.

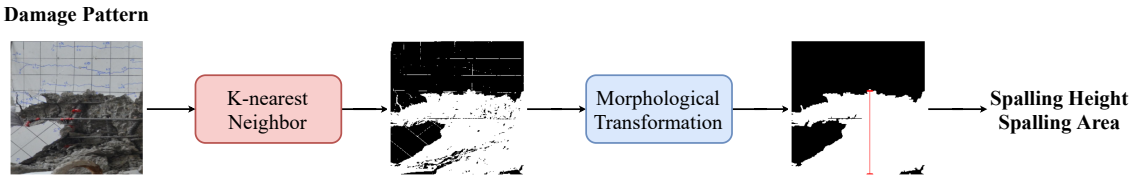

Figure 3.8: Proposed computer-vision based segmentation method for assessing spalling height and area.

3.5 Network Training

In this investigation, the proposed network architecture is realized utilizing Python 3 in conjunction with PyTorch [66] version 2.2.2, supported by CUDA 12.4, and operated on Rocky Linux 8.9. The computational experiments are conducted using an NVIDIA RTX A6000 GPU, equipped with 10,752 CUDA cores functioning at a base clock frequency of 1.455 GHz and endowed with 48 GB of GDDR6 memory.

doi:10.6342/NTU202402878

Chapter 4 Result and Discussion

In this chapter, we present both quantitative and qualitative evaluations for finite element simulation, hysteresis behavior prediction, damage index prediction, and damage pattern generation. First, in Section 4.1, we presents the simulated results of our proposed finite element modeling process by OpenSeesPy. The simulated results will serve as the input of HysGRU in the next section. In Section 4.2, the efficacy of the proposed HysGRU model is thoroughly evaluated by computing the RMSE and NRMSE of the entire hysteresis loops and reversal points. Furthermore, the potential advantages of integrating the simulation outcomes are explored to enhance the assessment.

In Section 4.3, we trained the DI prediction network to predict the corresponding damage index using authentic images and subsequently evaluated the performance of the model using the R^2 score. Finally, in Section 4.4, we present the findings of the damage patterns forecasting. To quantitatively assess generation performance, we employ the Peak Signal-to-Noise Ratio (PSNR), Structural Similarity Index (SSIM) and Fréchet Inception Distance (FID) [67] as similarity metrics to assess the fidelity of the damage patterns produced by the generator to evaluate the training stability and convergence. In addition, we calculate R^2 scores using synthetic data from the predictions of the corresponding DI values. As the pre-trained model uses authentic data, a higher similarity of the generated images to the real ones is expected to ensure similar downstream performance [68].

doi:10.6342/NTU202402878

4.1 Finite Element Simulation

For the finite element simulation, we assess the performance by computing the normalized root mean square error (NRMSE), thereby reducing the impact of scale variations among distinct hysteresis loops. As mentioned, bridge columns are susceptible to three primary modes of failure, i.e., flexural, flexural-shear, and shear. Within the domain of bridge engineering design, protocols typically emphasize mitigating shear failure while permitting the occurrence of flexural failure to balance budget constraints and safety considerations. In the modeling of hysteretic behavior, it is imperative to accurately predict the response at each reversal point of the drift ratio. Consequently, the NRMSE was calculated for the entirety of the hysteresis loop as well as for each individual reversal point. Table 4.1 presents the NRMSE of the simulated hysteresis responses compared to the experimental hysteresis loops in various types of failure. As evidenced in Table 4.1, accurate modeling of hysteretic behaviors in flexural-shear and shear failure modes presents a substantial challenge.

Table 4.1: Normalized root mean square error of the simulated outcomes in comparison to the experimental hysteresis loops across various failure types.

Failure Type	# of Loops	NRMSE (%)↓	
		Entire Loop	Reversal Points
Flexural	123	10.48	10.85
Flexural-Shear	22	15.01	12.81
Shear	15	23.86	27.89
Total	160	12.12	12.44

Figure 4.1 demonstrates the simulation results for the bridge specimens exhibiting flexural failure. The hysteresis loops depicted in the figure reveal wide loops indicative of substantial energy dissipation. The simulation is capable of approximating both the geometry and the strength of the hysteretic loops. Although the initial stiffness and yield

doi:10.6342/NTU202402878

points are well captured, the post-yield behavior, which includes the gradual softening and potential strength degradation, is less accurately modeled. This discrepancy can be attributed to the simplified assumptions made regarding the stress-strain relationship of materials and the inability to fully account for complex interactions such as bond-slip effects between concrete and reinforcing steel, and the influence of cyclic loading history. As a result, the predicted residual strength and the rate of stiffness degradation might differ from experimental observations.

Figure 4.2 and Figure 4.3 describes the simulation outcomes for the bridge specimens that show flexural shear and shear failure, respectively. In the case of flexural-shear failure, the simulation inadequately captures the interaction between flexural and shear mechanisms, resulting in a less accurate depiction of the hysteretic loops. The inherent complexity of combining bending and shear responses within a single model leads to difficulties in predicting the progressive degradation observed in the experiments. For shear failure, the limitations of simulation are even more evident. The fragile nature of shear failure, characterized by sudden strength degradation and minimal post-peak deformation, poses significant challenges for the proposed modeling approaches. For these two types of failure, the proposed method fails to accurately represent the overall hysteretic behavior. Consequently, to address these challenges, we investigate deep learning methodologies with the incorporation of simulation framework. Our objective is to leverage deep learning algorithms to correct the discrepancies observed between the simulation predictions and the experimental results.

doi:10.6342/NTU202402878

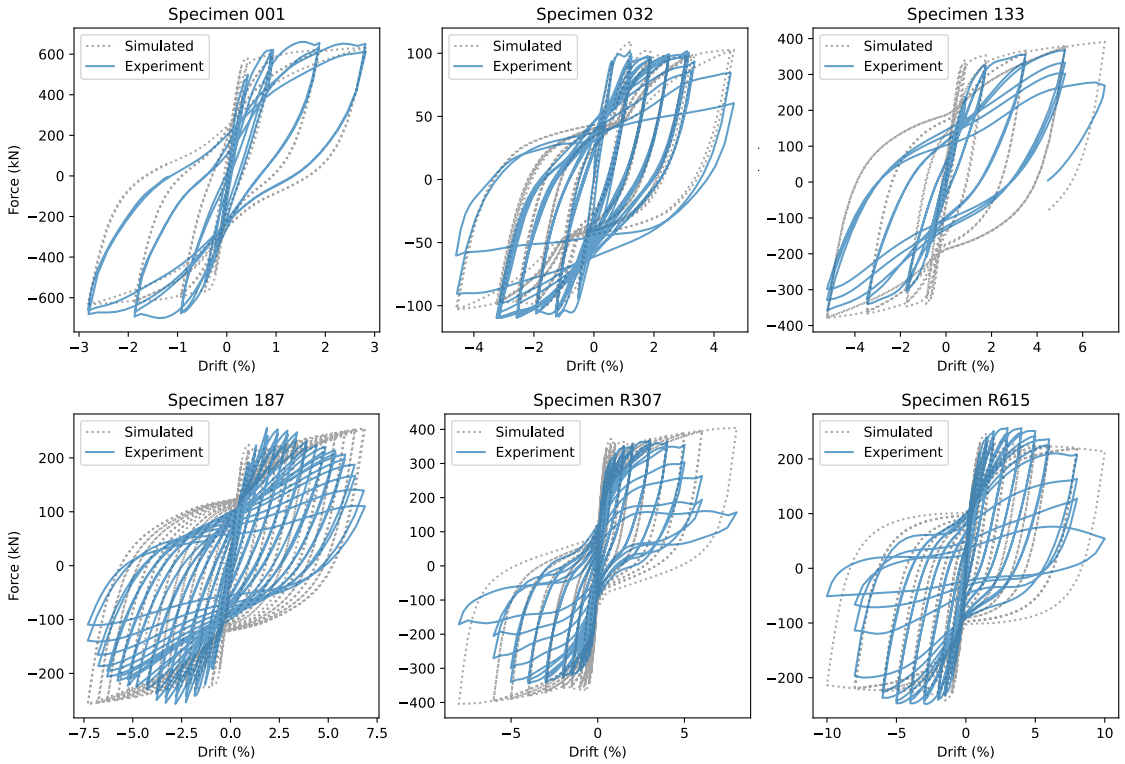

Figure 4.1: Simulation results from the specimens in hysteresis database with flexural failure.

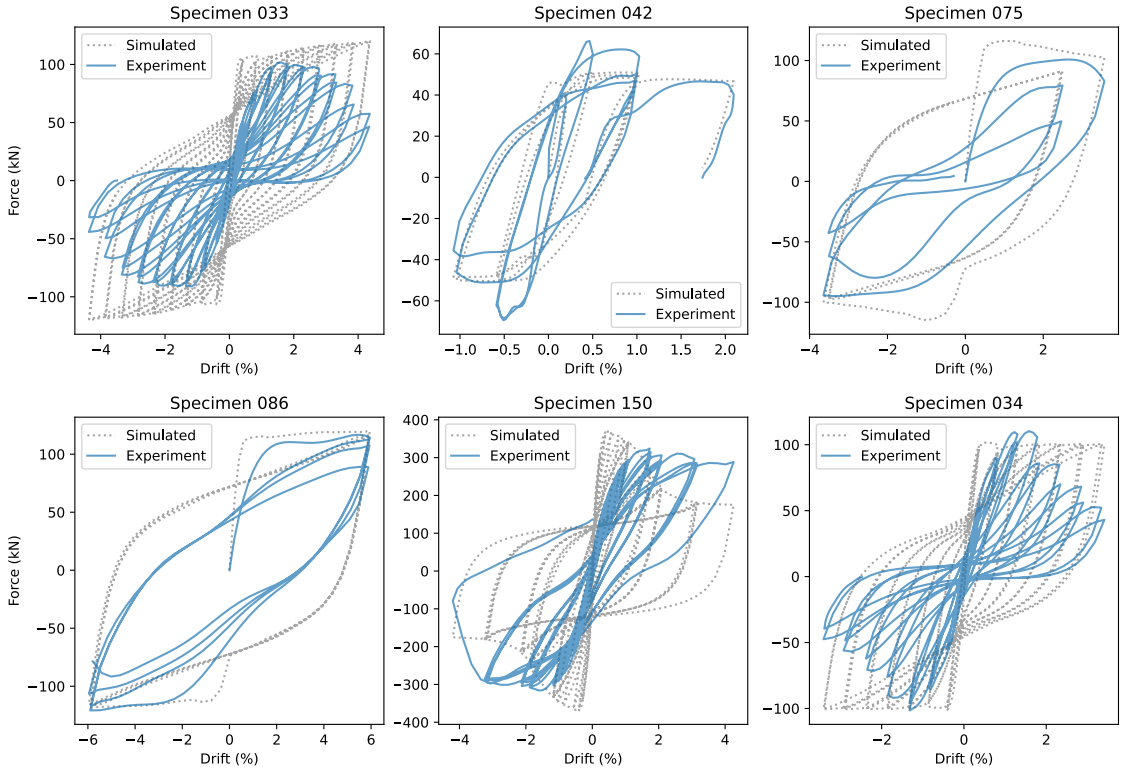

Figure 4.2: Simulation results from the specimens in hysteresis database with flexural-shear failure.

doi:10.6342/NTU202402878

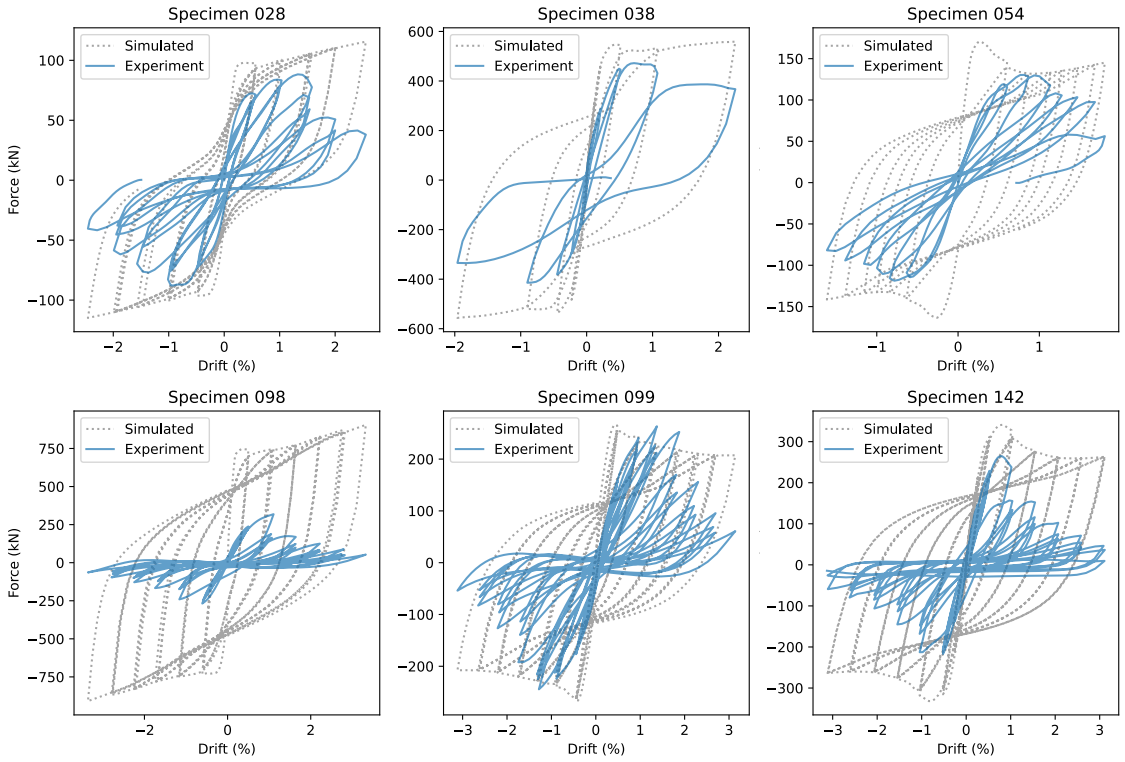

Figure 4.3: Simulation results from the specimens in hysteresis database with shear failure.

4.2 Hysteresis Behavior Prediction

Table 4.2 compares four training setups for HysGRU to predict the hysteresis loops, each with unique training configurations. The ablation study is conducted to evaluate the influence for involvement of simulation, force normalization, and force unit. In Exp1, simulation is not involved, force normalization is not applied, and the force unit is kilonewton (kN). This configuration is set as the baseline to compare the performance of the other setting. Exp2 employs a force unit of meganewton (MN) to rigorously assess the effects of the selected force unit. For Exp3, the integration of simulation results serves to inform the model with physics constraints derived from finite element analysis. Furthermore, leveraging the simulation results, we endeavor to normalize the force in Exp4 using the maximum response derived from the simulation to facilitate more effective model convergence. Consistent with finite element simulations, the root mean square error (RMSE)

doi:10.6342/NTU202402878

metric is adopted for evaluation. Furthermore, we evaluate the error for each failure type within the validation dataset, thereby computing the Normalized Root Mean Square Error (NRMSE) to reduce scaling effects derived from the hysteresis loops across distinct failure types. A thorough assessment is conducted to determine the impact across various failure modes.

Table 4.2: The setup of ablation study to assess the influence of integrating simulation, force normalization, and force unit on the performance of the proposed HysGRU.

ID	Simulation Involved	Force Normalization	Force Unit
Exp1	✗	✗	kN
Exp2	✗	✗	MN
Exp3	✓	✗	MN
Exp4	✓	✓	None

4.2.1 Quantitative Evaluation

As delineated in Table 4.3, the ablation study can be conducted to evaluate the consequences of integrating simulation, normalization, and force unit. Initially, for all experimental scenarios, the proposed HysGRU demonstrably mitigates the error relative to the outcomes derived solely from simulation, resulting in over 40% reduction in RMSE. A detailed examination of the results from Exp1 and Exp2 reveals that the incorporation of the force unit MN produces a notable decrease in error throughout the entire loop and at the reversal points by approximately 16% and 23% compared to Exp1, respectively. Furthermore, a comparative analysis of Exp2 and Exp3 reveals that the incorporation of simulation results can markedly enhance performance, as evidenced by the reduction of the error throughout the loop from 41.46 kN to 32.33 kN, corresponding to an approximate 22% reduction. Moreover, the results obtained from Exp3 and Exp4 suggest that the normalization of force using the maximum simulated force can further enhance the model

doi:10.6342/NTU202402878

performance. This improvement is evidenced by the reduction in the RMSE associated with the response for the entire loop, which decreased from 32.33 to 31.51 kN. The ablation study indicates that the model, which integrates simulation outcomes and normalizes force using the maximum simulated force, demonstrates superior performance across all training configurations. In comparison to results derived solely from simulation, the proposed approach achieves a reduction in RMSE for the entire loop from 82.88 kN to 31.51 kN, amounting to an approximate decrease of 62.0%. At the reversal points, the RMSE is reduced from 101.25 kN to 40.79 kN, which corresponds to a reduction of approximately 59. 7%.

Table 4.3: Validation RMSE for validation data computed from the HysGRU under diverse training configurations. Noted that the HysGRU trained with Exp4 have the optimal performance compared with the other experiments.

ID	RMSE (kN)↓	
	Entire Loop	Reversal Points
Purely Simulation	82.88	101.25
Exp1	49.09	73.28
Exp2	41.46	56.17
Exp3	32.33	42.95
Exp4	**31.51**	**40.79**

For a comprehensive analysis of the impact of different failure types, Table 4.4 delineates the NRMSE computed using the validation dataset encompassing varied failure types. The table demonstrates that the HysGRU with Exp4 configuration exhibits optimal performance under flexural and flexural-shear failure conditions. Conversely, the HysGRU is insufficient in accurately capturing the hysteretic behavior under shear failure conditions. Under conditions of shear failure, the HysGRU with the Exp2 configuration demonstrates superior performance, indicating its enhanced predictive capability in the absence of simulation data. The phenomenon may result in substantial discrepancies between the simulation and experimental outcomes. Additionally, the shear data comprises

doi:10.6342/NTU202402878

only five specimens within the validation dataset, potentially introducing significant bias in the evaluation.

Table 4.4: Validation NRMSE for various failure types computed from the HysGRU under diverse training configurations.

ID	NRMSE(%)					
	Flexural		Flexural-Shear		Shear	
	Entire	Reversal	Entire	Reversal	Entire	Reversal
Sim.	11.22	11.73	14.97	14.05	30.88	32.43
Exp1	5.16	7.41	4.83	6.52	7.57	10.64
Exp2	5.02	6.27	5.12	7.00	**6.83**	**8.31**
Exp3	3.86	4.66	5.34	6.52	7.59	12.28
Exp4	**3.39**	**3.95**	**5.09**	**6.37**	10.85	16.91

Figure 4.4, Figure 4.5, and Figure 4.6 present the NRMSE of individual specimens exhibiting flexural, flexural-shear, and shear failure, evaluated at reversal points within the validation dataset. It is evident that in forecasting the hysteresis loops of bridge columns undergoing flexural failure, the integration of simulation and normalization methodologies markedly reduces the prediction error in comparison to alternative training configurations. With regard to flexural-shear failure modes, the data reveal that the forecasted errors exhibit uniformity across the various training configurations, thereby indicating the absence of any discernible benefit from the integration of simulation results. In instances of shear failure, the aforementioned phenomenon is observed with heightened prominence. The model excluding simulation may exhibit superior performance, indicating that the model becomes confused when the simulation introduces significant mispredictions.

4.2.2 Qualitative Evaluation

Figure 4.7 illustrates the predictive analysis encompassing four configurations of the hysteretic response exhibited by bridge columns under conditions of flexural failure. As illustrated in Figure 4.7b, the HysGRU model utilizing the Exp1 configuration exhibits

doi:10.6342/NTU202402878

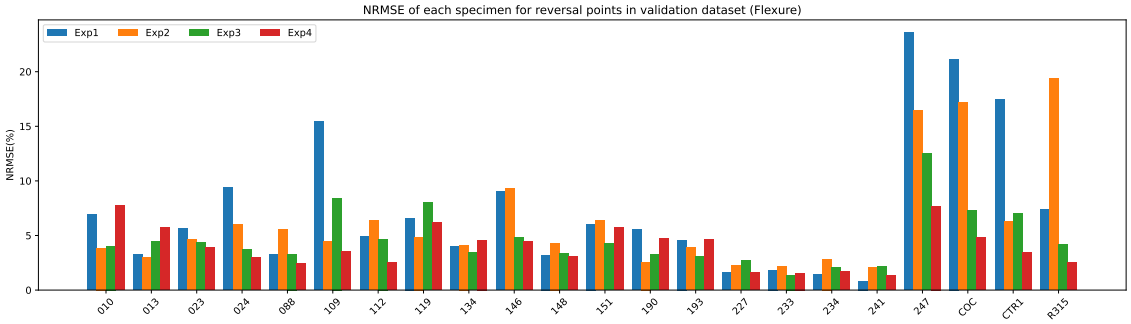

Figure 4.4: NRMSE of individual specimens exhibiting flexural failure, evaluated at reversal points within the validation dataset.

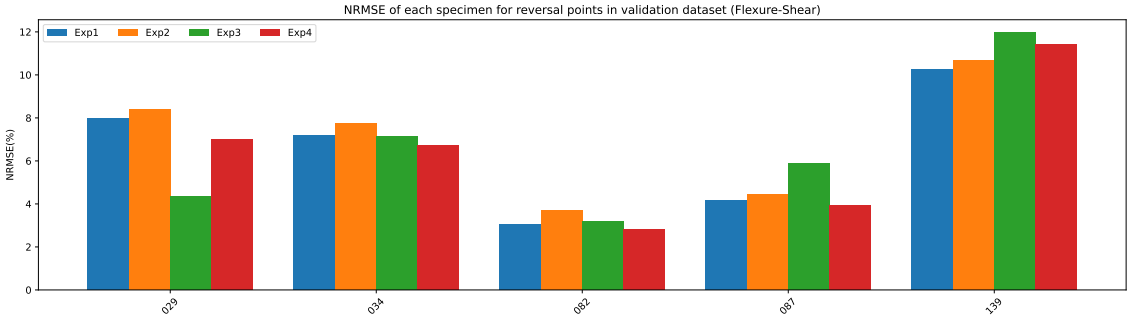

Figure 4.5: NRMSE of individual specimens exhibiting flexural-shear failure, evaluated at reversal points within the validation dataset.

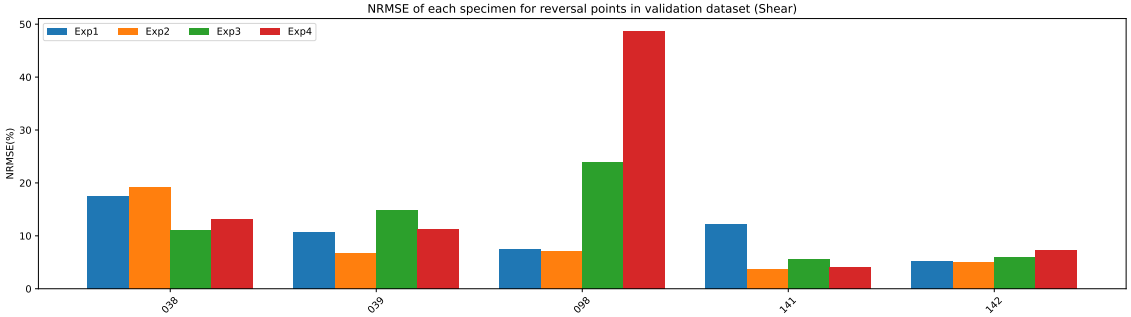

Figure 4.6: NRMSE of individual specimens exhibiting shear failure, evaluated at reversal points within the validation dataset.

doi:10.6342/NTU202402878

convergence challenges, resulting in the occurrence of upper and lower boundaries within the prediction. Owing to the force unit is quantified in kilonewton (kN) and the dataset encompassing a force magnitude spanning approximately from 0 to 1000 kN, the model may encounter obstacles to achieve convergence. Furthermore, as evidenced by Figure 4.7a and Figure 4.7b, the integration of simulation results can substantially improve the precision in predicting both the morphological features and the peak magnitudes. Additionally, normalizing the force by the maximum response observed in the simulations can enhance the precision of the predicted response at each reversal point.

Figures 4.8 and 4.9 present the forecasted outcomes for bridge columns under flexural-shear and shear conditions. In comparison with the predictive results for flexural columns, the predictions under these two failure modes exhibit inferior performance. Despite the observed limitations, the HysGRU algorithm shows promise in capturing key aspects of the complex hysteretic response in flexural-shear and shear failures. For flexural-shear columns, the algorithm reasonably approximates the initial stiffness and peak strength, though it struggles with the accurate portrayal of post-peak behavior and the transition from flexural to shear dominance. In the case of shear failure, the HysGRU algorithm demonstrates the ability to replicate initial pinching and stiffness degradation. However, rapid loss of strength poses significant challenges, leading to discrepancies between predicted and actual responses. Despite these limitations, the generation of damage patterns is primarily concentrated on flexural bridge columns. Consequently, the proposed HysGRU algorithm demonstrates adequate performance.

doi:10.6342/NTU202402878

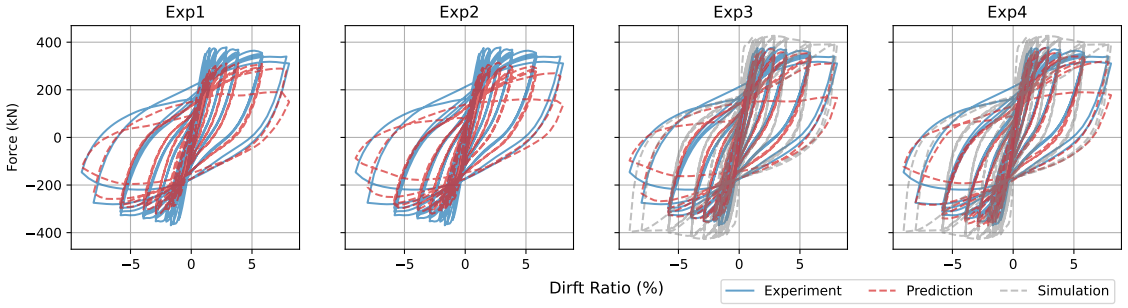

(a) PEER Specimen 146

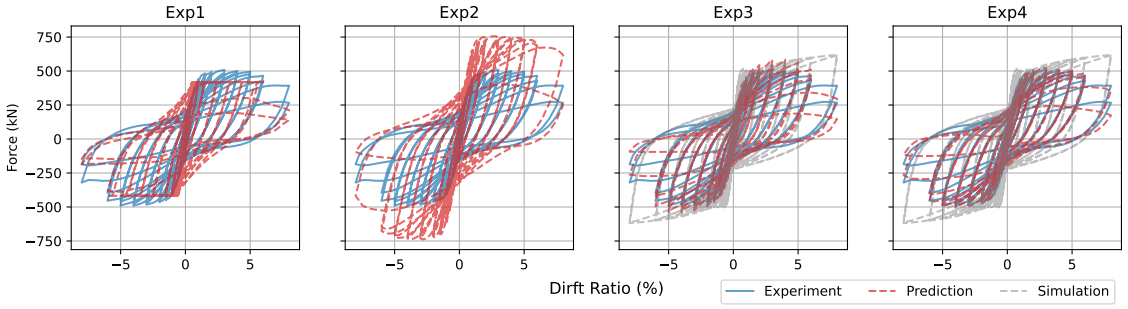

(b) NCREE Specimen R315

Figure 4.7: The predicted hysteresis loops for (a) PEER specimen 010 [69] and (b) NCREE specimen R315 [4] demonstrating flexural failure.

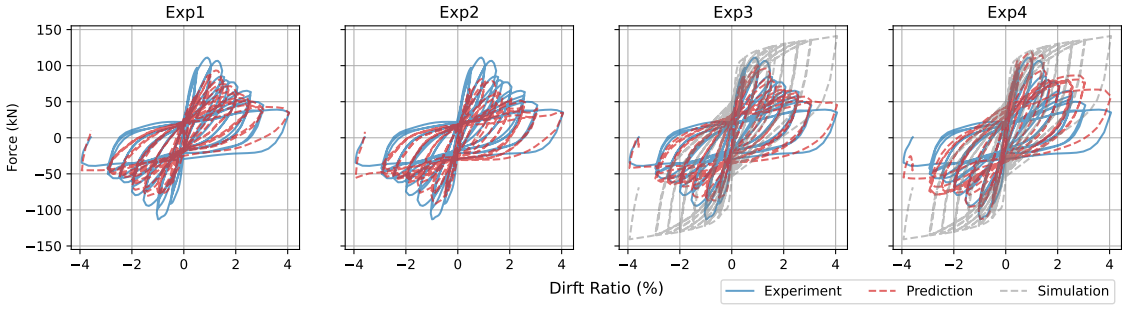

(a) PEER Specimen 029

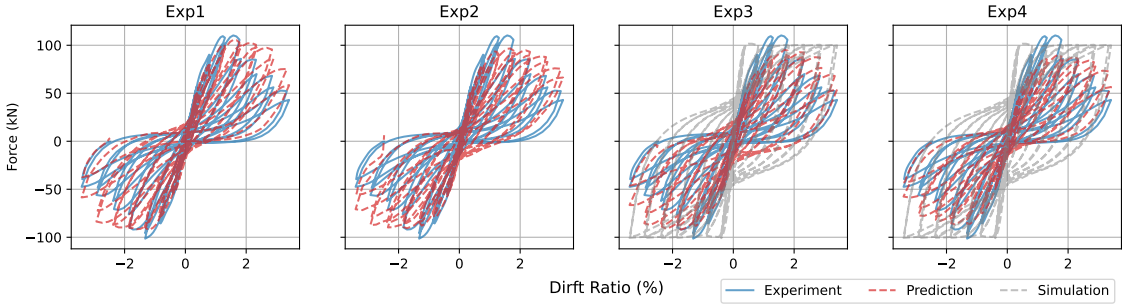

(b) PEER Specimen 034

Figure 4.8: The predicted hysteresis loops for (a) PEER specimen 029 [70] and (b) PEER specimen 034 [71] demonstrating flexural-shear failure.

doi:10.6342/NTU202402878

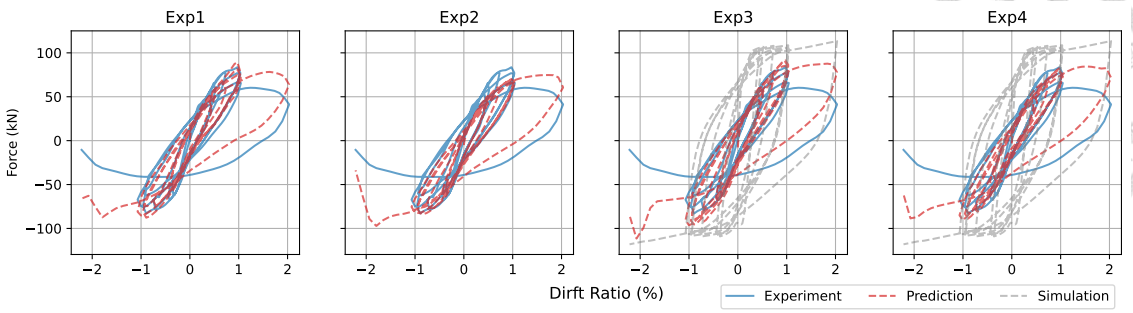

(a) PEER Specimen 039

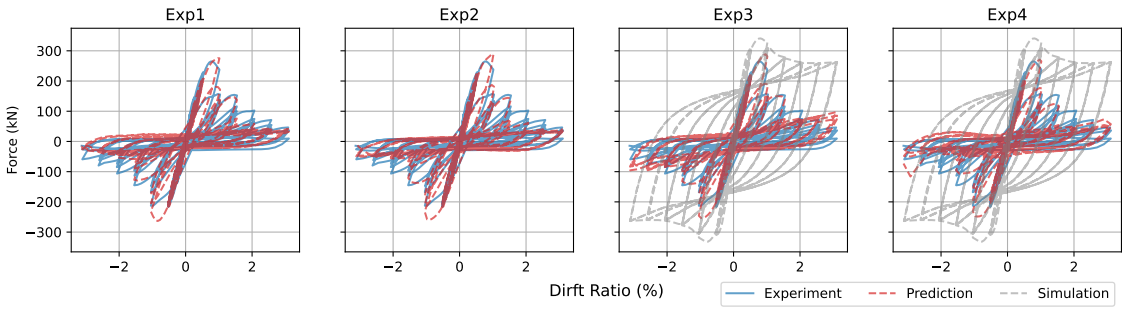

(b) PEER Specimen 142

Figure 4.9: The predicted hysteresis loops for (a) PEER specimen 039 [72] and (b) PEER specimen 142 [73] demonstrating shear failure.

4.3 Damage Index Prediction

The damage mechanisms of reinforced concrete bridges are intricate; for instance, while the damage patterns may appear similar, the structural performance and strength exhibit significant variations. As a result, in this section, we present the proposed DI prediction network to quantify the extent of damage to bridge columns. By taking damage patterns and column design parameters into consideration, the proposed network is able to predict the corresponding DI, allowing to assess the structural performance based on visual imagery. Upon the establishment of the damage pattern database, the prediction network is subsequently trained utilizing authentic damage patterns obtained from cyclic loading experiments. In this task, we adopt the coefficient of determination regression score (R^2) to evaluate the performance of the model. The R^2 score can be calculated

doi:10.6342/NTU202402878

using the following equation.

$$R^2 = 1 - \frac{\sum_i (y_i - \hat{y}_i)^2}{\sum_i (y_i - \bar{y}_i)^2} \tag{4.1}$$

where y_i is the ground truth; $\hat{y}_i$ is the predicted value; $\bar{y}_i$ is the mean of the ground truth.

Figure 4.10 presents the verification for regression accuracy of the damage index. The proposed DI prediction network can achieve R^2 score 0.9970 and 0.9887 for the training and validation dataset, respectively. The R^2 score for the validation set was marginally lower than that of the training set, indicating that the model demonstrated no evidence of overfitting. This observation implies that the model sustained robust stability across diverse samples within both the training and validation datasets.

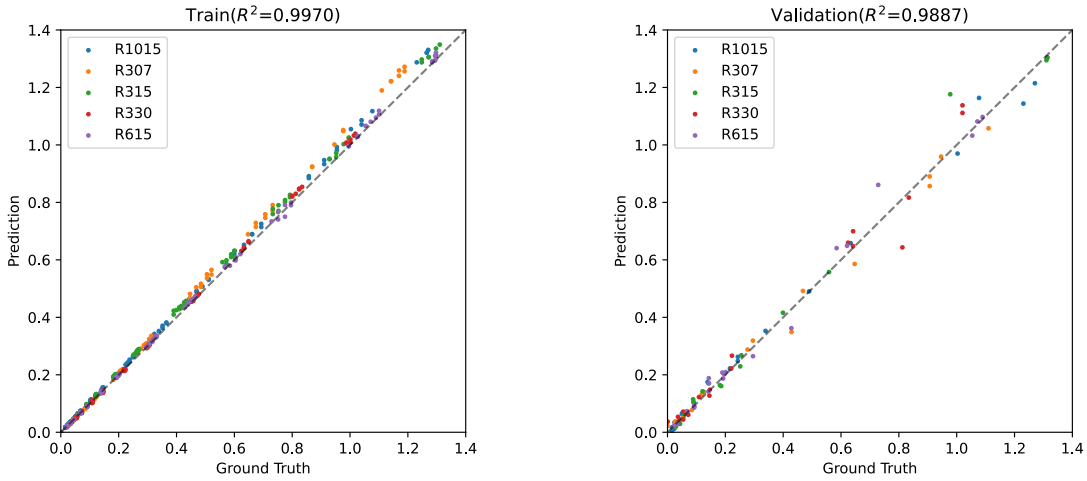

Figure 4.10: Verification for regression accuracy of the damage index.

The Multi-Head Attention mechanism in VIT facilitates focused attention on relevant segments of the image. Adhering to the model architecture illustrated in Figure 3.7, the attention score for the class token is calculated with respect to all other patches. The model selectively attends to image regions that are semantically significant for DI prediction. The architecture of ViT-base contains 12 transformer encoders. Figure 4.11 presents

doi:10.6342/NTU202402878

the visualization of the attention maps for each layer. The predicted DI value is 1.0816, whereas the ground truth is 1.0715, resulting in an error of approximately 0.9%. From the visualization of attention maps, it is evident that the DI prediction network concentrates on the region of concrete spalling, which serves as a critical indicator of structural damage to the bridge column. Thus, the evaluation demonstrates that the proposed DI prediction network capably quantifies structural damage with precision utilizing vision-based imagery.

It is imperative to acknowledge that the training and validation datasets were exclusively comprised of images derived from the five specified specimens, specifically R307, R315, R330, R615, and R1015. Conversely, the test dataset was exclusively constituted of images from specimen CTR1, thereby ensuring that the network had no prior exposure to the damage patterns exhibited by CTR1. With respect to each cyclic loading test, there exist distinct environmental variables, including illumination conditions and anchor point positioning. These variables may introduce considerable bias. This limitation culminates in a diminished R^2 score, approximating 0.5744, as observed in the performance metrics of the testing dataset. For future implementations, it is imperative to augment the dataset to enhance the generalization proficiency of the DI prediction network. For the evaluation of HysGAN, given that HysGAN is also trained utilizing identical training and validation datasets, the resultant synthetic damage patterns are anticipated to manifest similar environmental factors in the empirical damage patterns. This uniformity facilitates the proposed DI prediction network in rigorously assessing the performance of HysGAN in the subsequent section.

doi:10.6342/NTU202402878

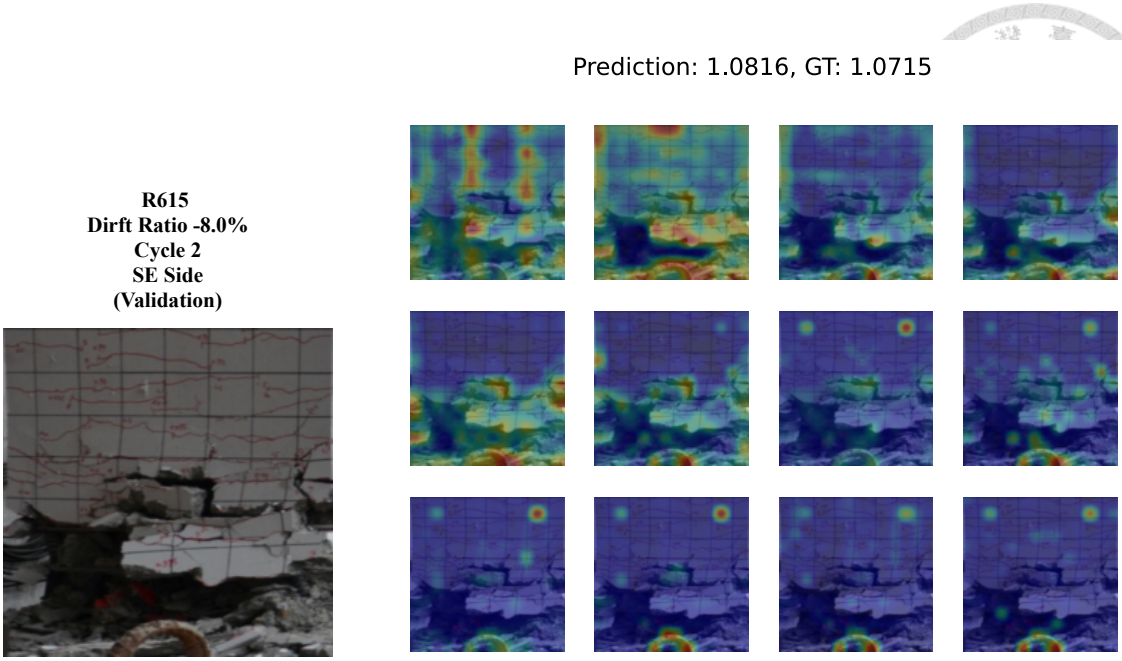

Figure 4.11: The attention maps derived from the 12 layers of the transformer encoders in the proposed DI prediction network, demonstrate that model focus on the damaged regions of bridge columns.

4.4 Damage Pattern Generation

In this section, we present the results of the generation from the proposed HysGAN. We first introduce the evaluation metrics for assessing the similarity of the damage patterns. However, intuitive similarity metrics might not accurately capture the consistency of bridge damage conditions, we therefore assess the generation performance by predicting the Damage Index (DI) using a pre-trained DI prediction network from the previous section, which has been trained on authentic images. Subsequently, both quantitative and qualitative evaluations have been systematically presented.

4.4.1 Evaluation Metrics

The Peak Signal-to-Noise Ratio (PSNR) serves as a pivotal metric for evaluating the quality of reconstructed or compressed images. This metric quantifies the relation-

doi:10.6342/NTU202402878

ship between the maximum possible intensity of the original image and the intensity of the discrepancies found between the original and the compressed or reconstructed image. Measured in decibels (dB), a higher PSNR value indicates superior image quality, characterized by minimal noise and distortion. PSNR is especially beneficial within the domains of image processing, compression, and transmission, offering a straightforward quantitative assessment of image fidelity. The Peak Signal-to-Noise Ratio (PSNR) metric can be mathematically formulated as follows:

$$PSNR(\boldsymbol{x}, \boldsymbol{y}) = 20 \log_{10}(\frac{MAX_I}{\sqrt{MSE(\boldsymbol{x}, \boldsymbol{y})}}) \tag{4.2}$$

where $\boldsymbol{x}$ and $\boldsymbol{y}$ denote the image pairs employed for the computation of the PSNR; MAX_I signifies the maximum possible pixel intensity value (commonly set to 255); $MSE(\boldsymbol{x}, \boldsymbol{y})$ represents the mean squared error computed from the pixel values of the two images.

The Structural Similarity Index (SSIM) [74] represents a perceptual metric employed to evaluate the quality of images through the assessment of similarity between paired images. Contrasting traditional approaches based on pixel-wise deviations, SSIM investigates alterations in structural information by incorporating considerations of luminance, contrast, and structural composition. It generates a score ranging from -1 to 1, with a value of 1 that means optimal structural similarity. SSIM is extensively utilized within the image processing and computer vision domains to measure image quality and substantiate image generation models, given its strong concordance with human visual perception. The SSIM can be calculated by the following equation:

$$SSIM(\boldsymbol{x}, \boldsymbol{y}) = l(\boldsymbol{x}, \boldsymbol{y}) c(\boldsymbol{x}, \boldsymbol{y}) s(\boldsymbol{x}, \boldsymbol{y}) \tag{4.3}$$

doi:10.6342/NTU202402878

with

$$l(\boldsymbol{x}, \boldsymbol{y}) = \frac{2\mu_x\mu_y + C_1}{\mu_x^2 + \mu_y^2 + C_1} \tag{4.4}$$

$$c(\boldsymbol{x}, \boldsymbol{y}) = \frac{2\sigma_x\sigma_y + C_2}{\sigma_x^2 + \sigma_y^2 + C_2} \tag{4.5}$$

$$s(\boldsymbol{x}, \boldsymbol{y}) = \frac{\sigma_{xy} + C_3}{\sigma_x\sigma_y + C_3} \tag{4.6}$$

where $\boldsymbol{x}$ and $\boldsymbol{y}$ represent the image pairs utilized to compute the SSIM; μ_x and μ_y denote the mean intensity values of the two images; σ_x and σ_y correspond to the variances of the image intensities; and C_1, C_2, and C_3 are constants designed to prevent division by zero. $l(\boldsymbol{x}, \boldsymbol{y})$, $c(\boldsymbol{x}, \boldsymbol{y})$, and $s(\boldsymbol{x}, \boldsymbol{y})$ evaluate the similarity in terms of luminance, contrast, and structural composition, respectively.

Unlike PSNR and SSIM which are calculated by comparing the similarity from each image, the Fréchet Inception Distance (FID) assess the generation performance by calculating the distance between two data distributions. The FID score [67] is extensively utilized in the domain of image generation to quantify the divergence between the feature vectors of authentic and synthetic images. The Inception V3 network [75] serves as the feature extractor, producing activations for both real and synthetic images, which are subsequently modeled as multivariate Gaussian distributions. By inputting synthetic images and authentic damage patterns into the Inception V3 network, we derive feature vectors that constitute two distinct multivariate Gaussian distributions, encapsulating the synthetic and real damage patterns, respectively. The FID score is computed to determine the separation between these two distributions. The equation governing the FID score is delineated as follows:

$$FID = ||\boldsymbol{\mu_1} - \boldsymbol{\mu_2}||_2^2 + Trace\big(\boldsymbol{\sigma_1} + \boldsymbol{\sigma_2} - 2\sqrt{\boldsymbol{\sigma_1\sigma_2}}\big) \tag{4.7}$$

doi:10.6342/NTU202402878

where $\boldsymbol{\mu_1}$ and $\boldsymbol{\sigma_1}$ represent the mean and covariance matrix of the feature vectors derived from the training dataset, respectively, while $\boldsymbol{\mu_2}$ and $\boldsymbol{\sigma_2}$ denote the mean and covariance matrix associated with the feature vectors of the synthetic dataset. Consequently, lower FID scores signify that the synthetic images generated exhibit increased similarity, higher quality, and greater diversity in comparison to the authentic damage patterns.

PSNR, SSIM, and FID scores are employed to assess the similarity and quality of generated images. Nevertheless, these similarity metrics may not adequately evaluate the consistency of the damage states in bridge columns. Therefore, as previously mentioned, we also incorporated the DI prediction network to evaluate the generative performance by calculating the R^2 score for the synthetic damage patterns. It is important to note that the pretrained DI prediction network was trained using authentic images. Consequently, if the generated damage patterns exhibit high fidelity and realism, a higher R^2 score is anticipated. For training and validation datasets, the proposed HysGAN has the capability to predict almost identical patterns compared to the ground truth, since the column designs are observed during the training phase. However, for column designs that are excluded from the training dataset, accurately predicting the corresponding damage patterns poses significant challenges. Although PSNR and FID metrics provide insight into the training stability of the generative model, they are inadequate to assess the rationality of synthetic damage patterns due to substantial influences from variations in color and brightness. Therefore, the assessment focus shifts to evaluating the DI prediction, along with the quantification of the height and area of concrete spalling.

doi:10.6342/NTU202402878

4.4.2 Quantitative Evaluation

In order to rigorously assess the influence of condition type, loss function, and image resolution, various training configurations are established. To explain the impact of condition type, the initial control of the generator is attempted through the modulation of column design parameters along with the DI. This configuration is designated as the baseline for comparative analysis. Conversely, the latent feature derived from the HysGRU, trained with the Exp4 configuration in Section specified in 4.2.1, is used to establish the improvement of latent feature conditioning. Also, in this study, we also endeavor to evalute the influence of end-to-end training and adversarial training. In adopting end-to-end training, the discriminator is eliminated, enabling a direct end-to-end training approach. In this configuration, the conditioning parameters are fed directly into the generator to synthesize the corresponding images. The MSE between the generated images and the ground truth is then computed to optimize the model weights. For adversarial training, we compared the optimization results for different loss functions, including SGAN, RSGAN, and RaSGAN. Detailed loss functions for adversarial training are delineated in Section 3.3.

Table 4.5: Experiments for HysGAN with different training configurations with various condition types, loss functions, and image resolution.

ID	Condition Type	Training Approach	Image Resolution
Exp1	Column Design Parameters+DI	End-to-End	128
Exp2	Latent Feature	End-to-End	128
Exp3	Latent Feature	SGAN	128
Exp4	Latent Feature	RSGAN	128
Exp5	Latent Feature	RaSGAN	128
Exp6	Latent Feature	SGAN	512
Exp7	Latent Feature	RaSGAN	512

Table 4.6 presents the calculated PSNR, SSIM, FID and R^2 for HysGAN trained with

doi:10.6342/NTU202402878

various training configurations. In alignment with the database configuration described in Section 2.2, the training, validation, and test datasets correspond to different experimental scenarios. Specifically, the training, validation, and test datasets comprise data exhibiting observed column designs and conditions, observed column designs with unobserved conditions, and unobserved column designs with unobserved conditions, respectively. A comparative analysis between Exp1 and Exp2 reveals that the incorporation of latent features as conditional input significantly enhances training stability and generalizability. For the evaluation metrics, the PSNR and SSIM exhibit significant improvements, and the FID demonstrates a marked reduction. The phenomenon indicates an enhanced similarity and diminished noise levels in the synthetic training data compared to the authentic training data. Furthermore, the marked improvement in the R^2 score suggests that conditioning on latent features substantially enhances the generalizability of HysGAN.

In Exp3, we employed the SGAN loss function to implement the adversarial training protocol. In comparison to the results obtained in Exp2 and Exp3, a direct end-to-end training approach demonstrates superior performance in both training and validation datasets. This can be attributed to the fact that the damage patterns within these datasets are derived from identical cyclic loading tests. However, with regard to the testing dataset, the damage patterns originate from previously unobserved cyclic loading tests, which results in suboptimal performance when employing end-to-end training methods. The implementation of adversarial training enables HysGAN to accurately predict the decent damage patterns for previously unexamined column designs. Through the experiments Exp3, Exp4, and Exp5, various adversarial losses were evaluated. It is evident that the utilization of the relativistic discriminator enhances stability and quality during the training, validation, and testing phases, as indicated by the improvements in all metrics. In comparison to the RSGAN and

doi:10.6342/NTU202402878

RaSGAN loss functions, it is noticeable that the performance metrics on the training and validation datasets exhibit similarity. However, the integration of RaSGAN manifests a marked enhancement in the R^2 value when evaluated in the test dataset.

Moreover, it is apparent that damage patterns captured at higher image resolutions can provide a more detailed depiction of bridge column damage. Nevertheless, adversarial training at higher resolutions frequently encounters the issue of mode collapse. Mode collapse refers to a phenomenon wherein the generator produces a singular pattern that consistently deceives the discriminator. Compared with the outcomes obtained from Exp6 and Exp7, it is evident that both SSIM and FID metrics exhibit substantial improvement when employing a relativistic discriminator. This observation suggests that the application of the relativistic loss function significantly enhances the stability of the training process at elevated image resolutions. Ultimately, it can been observed that, under identical training parameters, an increase in image resolution enhances the precision of DI estimation. This enhancement can be attributed to the higher level of detail provided by higher resolution images, which more accurately depict damage phenomena such as rebar buckling, rebar fractures, and other damage scenarios.

Table 4.6: Performance metrics for multiple loss functions and image sizes across training, validation, and test datasets. Metrics include PSNR, SSIM, FID, and R^2. Noted that the HysGAN demonstrates variations in the generation of damage patterns within the test dataset under diverse environmental conditions when compared to the ground truth, thereby necessitating the exclusive presentation of the R^2 metric.

ID	Training				Validation				Test
	PSNR↑	SSIM ↑	FID ↓	R^2 ↑	PSNR↑	SSIM ↑	FID ↓	R^2 ↑	R^2 ↑
Exp1	23.80	0.88	45.69	0.85	21.31	0.80	61.98	0.87	0.37
Exp2	45.30	0.99	4.86	0.97	20.87	0.79	58.93	0.78	0.63
Exp3	18.82	0.81	68.52	0.82	19.35	0.73	97.40	0.68	0.66
Exp4	20.58	0.85	25.19	0.93	18.24	0.72	65.09	0.74	0.72
Exp5	18.17	0.80	36.32	0.92	16.14	0.67	77.40	0.71	0.84
Exp6	22.21	0.68	71.21	0.94	18.47	0.56	113.42	0.87	0.83
Exp7	20.93	0.79	37.31	**0.98**	17.82	0.64	82.53	**0.92**	**0.92**

doi:10.6342/NTU202402878

4.4.3 Qualitative Evaluation

Figure 4.12 presents the generation results with image resolution 128×128 under different conditions and the configurations of the loss function. The initial row shows the six distinct damage patterns from the training, validation, and testing datasets. Subsequently, from the second row to the final row, the table delineates the generated outcomes from HysGAN utilizing training configurations Exp1 through Exp5.

Initially, an examination of the second and third rows reveals that the integration of latent features can substantially enhance the image quality of the forecasted damage patterns. The damage patterns predicted in the second row utilize the column feature and DI as conditioning variables, leading to images of diminished clarity. Additionally, in the context of testing data featuring unobserved column designs, it is evident that end-to-end training methodologies fail to produce damage patterns consistent with the ground truth. Specifically, discrepancies are notable in the concrete spalling area and height.

By comparing the results from Ex1 to Exp2 and from Exp3 to Exp5, it can be observed that implementing the adversarial training process significantly enhances the generalizability of HysGAN, enabling it to predict the approximate damage patterns from the unobserved condition vector and column design, which correspond to validation data and testing data. By examining the comparison of three forms of adversarial loss, as illustrated in the final three rows, it is evident that the image quality, along with the predicted concrete area and height from Exp5, exhibits the closest similarity to the damage patterns derived from ground truth in training, validation and testing datasets.

Figure 4.13 illustrates the damage patterns synthesized by HysGAN using the Exp5 through Exp7 configurations. As demonstrated in the figure, the synthesized damage pat-

doi:10.6342/NTU202402878

terns exhibit an elevated level of detail in representing the damage conditions, including features such as fractured rebar and cracks. When contrasted with the generated outcomes from Exp6 and Exp7, no discernible differences are observed. This similarity suggests that the improvements made in the Exp7 configuration did not significantly enhance the visual quality of the damage patterns compared to Exp6. Nevertheless, based on the quantitative results described in the previous section, we advocate the utilization of HysGAN configured with latent feature conditioning, RaSGAN loss, and an image resolution of 512×512. This configuration was found to provide the best balance between computational efficiency and the accuracy of the synthesized damage patterns. The use of RaSGAN loss contributes to stabilizing the training process and improving the overall realism of the generated images by minimizing the discrepancy between real and synthetic samples. Furthermore, the high-resolution output ensures that even the smallest damage features are accurately captured, which is critical for applications requiring precise damage assessment.

Figure 4.14 illustrates the advanced damage assessment on the generative outcomes derived from the proposed HysGAN, which incorporates RaSGAN loss with latent feature conditioning. The spalling regions within the synthetic damage patterns were segmented utilizing the conventional computer vision methodologies described in Section 3.4. According to the grid size on the column surface, we can transfer the spalling height to centimeters. It can be observed that regardless of the resolution of the image, HysGAN is capable of predicting plausible damage patterns that correlate with real-world damage scenarios. Higher resolution damage patterns provide a more comprehensive description, such as the fracture and buckle of the longitudinal rebars. This demonstrates the ability of the proposed generative model to effectively process images at a resolution of 512×512.

doi:10.6342/NTU202402878

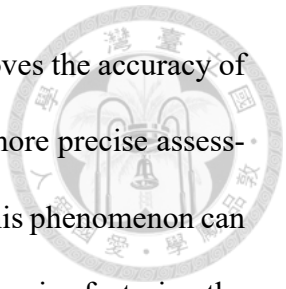

Furthermore, the generation of high-resolution damage patterns improves the accuracy of the DI prediction network by providing enhanced detail, allowing a more precise assessment of the DI through visual images and column structural design. This phenomenon can be observed in all the six examples presented in the figure. Under scenarios featuring the observed column design, the proposed HysGAN demonstrates the capability to generate damage patterns nearly indistinguishable from the ground truth. Consequently, the predicted spalling area and height align closely with the ground truth observations. However, it is evident that the synthetic results with a resolution of 128×128 exhibit limitations in accurately predicting the corresponding DI.

For the validation dataset, the proposed HysGAN has considered the column design but has not accounted for the latent features extracted from the corresponding drift ratio step during training. The proposed HysGAN demonstrates the capability to predict the unseen drift ratio step by integrating information derived from hysteresis loops. From the prediction in the fourth row of Figure 4.14, it is evident that, although the damage patterns differ, the predicted spalling area and height closely approximate the ground truth. On the other hand, for test datasets comprising unobserved column designs, the proposed methodology remains proficient in generating plausible damage patterns, although not entirely consistent with the ground truth. The findings underscore the method capacity to precisely synthesize damage profiles, particularly with regard to the height and area of concrete spalling, as well as in the accurate prognostication of the DI.

doi:10.6342/NTU202402878

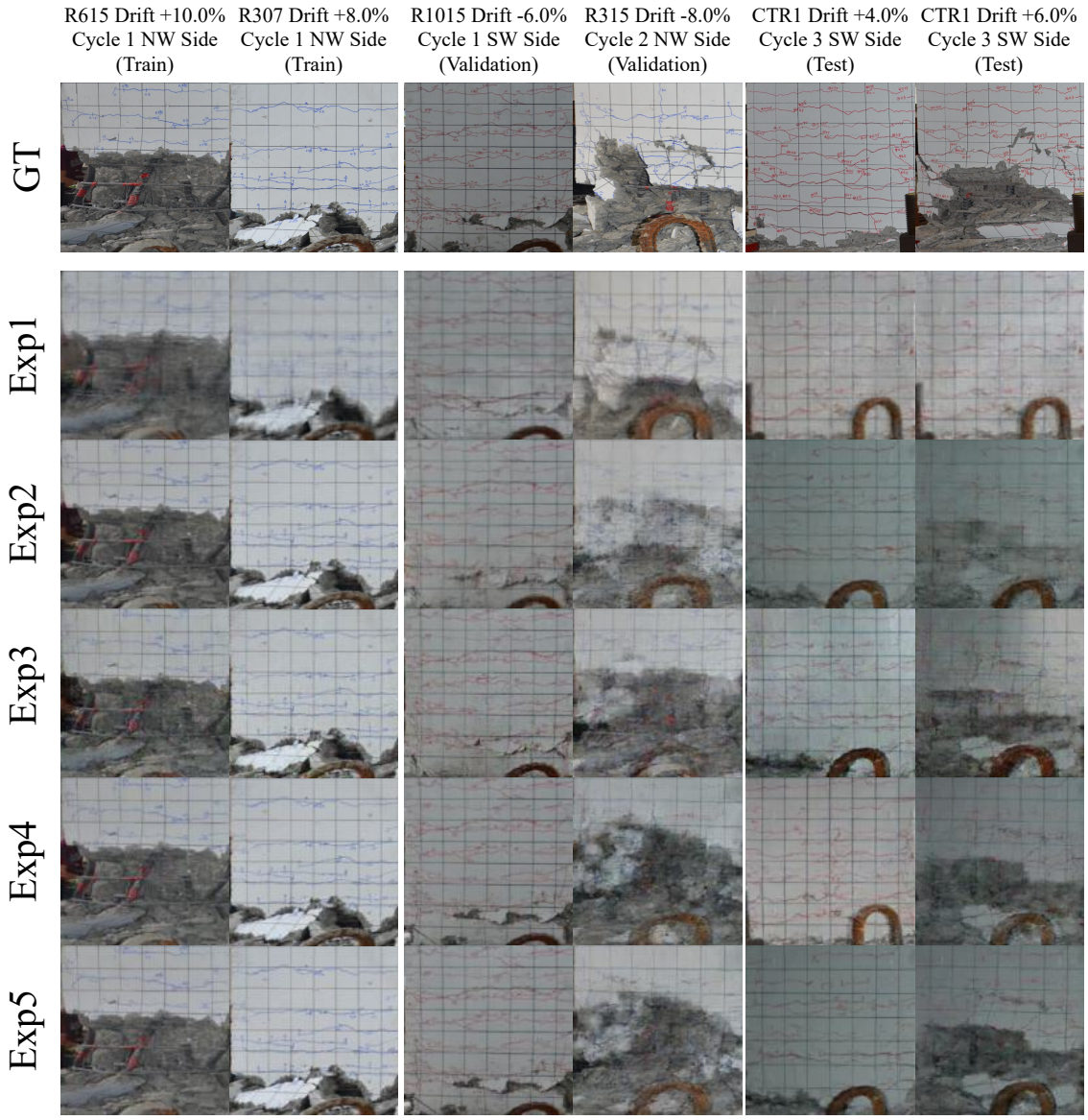

Figure 4.12: Generated damage patterns at an image resolution 128×128 under varying conditions and diverse loss function configurations. From top to bottom rows corresponding to the ground truth and Exp1 through Exp5, respectively.

doi:10.6342/NTU202402878

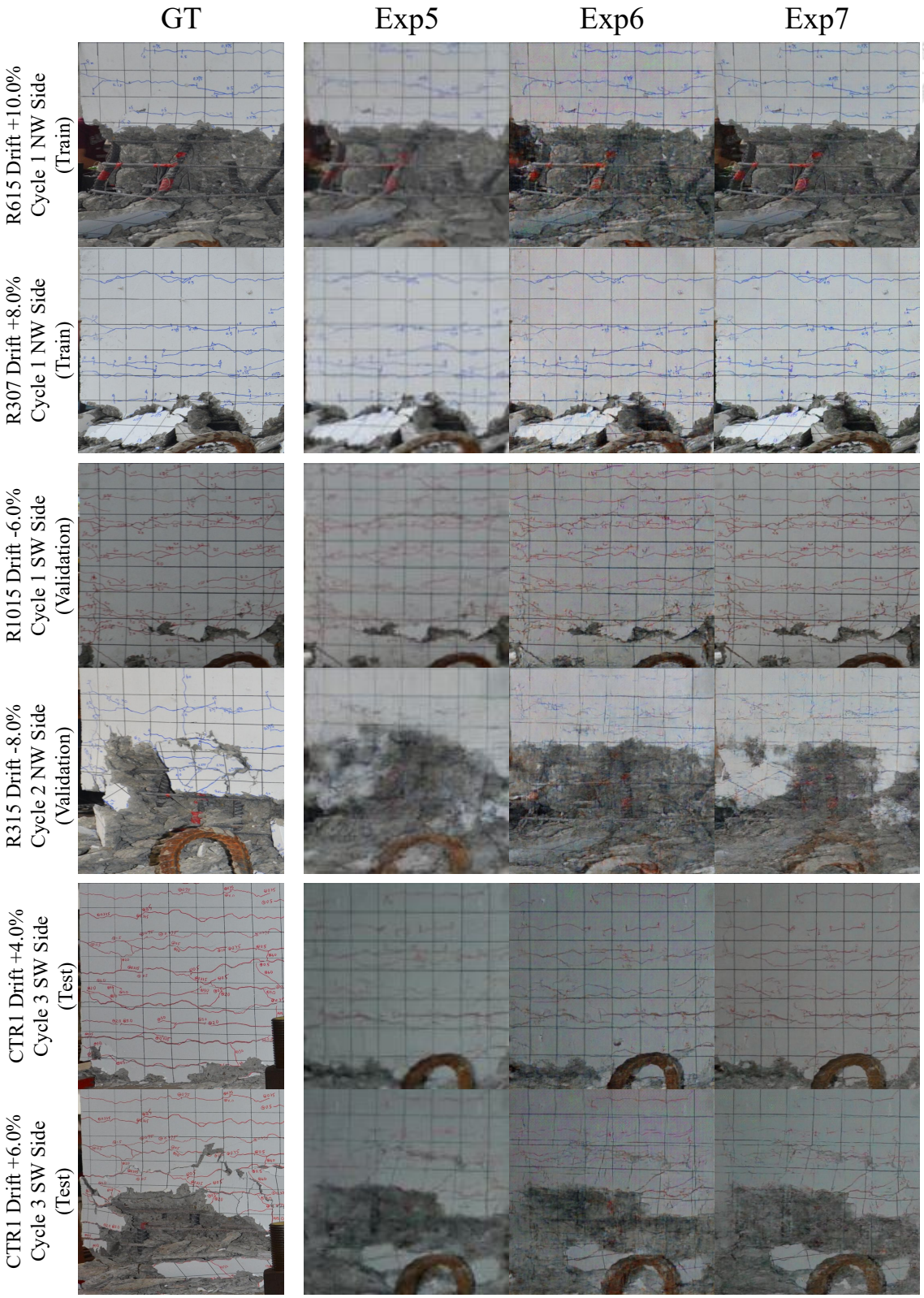

Figure 4.13: Generated damage patterns for HysGAN with Exp5 to Exp7 configurations. Noted that the HysGAN incorporating latent feature conditioning, RaSGAN loss, and a 512×512 image resolution exhibits superior performance.

doi:10.6342/NTU202402878

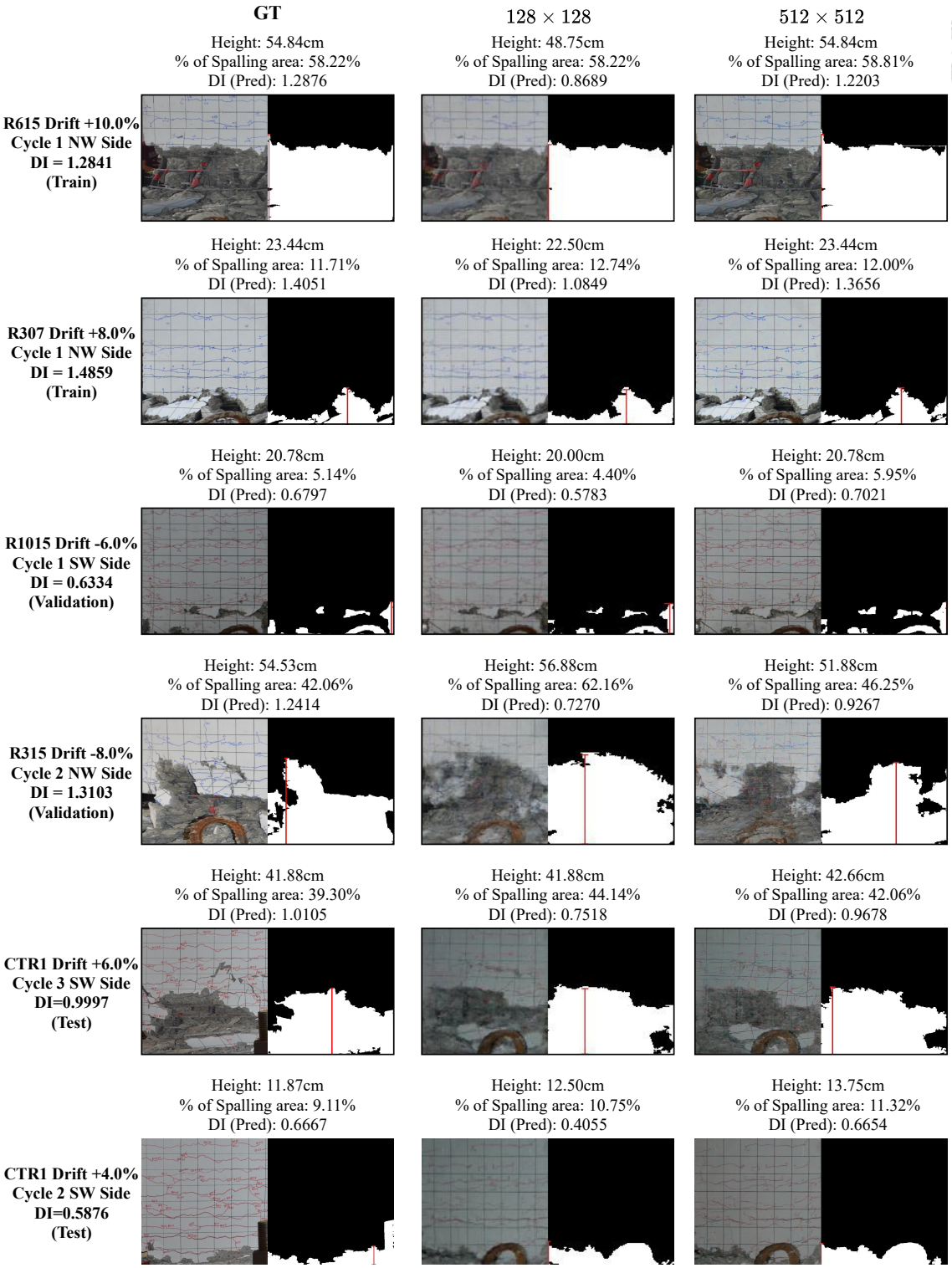

Figure 4.14: Rigorous assessment of the generative outcomes produced by HysGAN, which integrates RaSGAN and conditional latent features, at image resolutions of 128×128 and 512×512, focusing on the prediction of Damage Index (DI), concrete spalling height, and spalling area.

doi:10.6342/NTU202402878

Chapter 5 Conclusion

5.1 Summary

This study presents an innovative prognostic framework leveraging deep learning methodologies to evaluate the hysteretic response, damage distributions, and overall structural performance of RC bridge columns. The proposed hysteresis loop prediction network, HysGRU, is capable of accurately predicting hysteresis behaviors for all types of bridge failure, especially flexural failure. In addition to modeling the hysteretic behavior, the proposed damage patterns generative model, HysGAN, demonstrates the capability to predict corresponding damage patterns across all drift ratio stages within the hysteresis loops, thereby facilitating a comprehensive understanding of the damage mechanisms of bridge columns. Furthermore, we introduce a damage index (DI) prediction network designed to evaluate structural performance by utilizing visual imagery alongside column design parameters. Leveraging the proposed HysGRU and HysGAN models, engineers can predict seismic hysteretic behaviors and corresponding damage patterns based on specified column design parameters and selected drift ratios, allowing for a more efficient assessment of seismic design and structural capacity.

The significant conclusions derived from the study are enumerated as follows.

doi:10.6342/NTU202402878

1. The proposed HysGRU can successfully predict the hysteretic behavior of RC bridge column for all the training configurations, resulting in more than 40% reduction in RMSE.

2. By integrating simulation results and applying normalization techniques during the prediction of hysteresis loops, HysGRU attains an RMSE of 31.51 kN, representing an approximately 35% reduction relative to the baseline model.

3. The proposed damage index (DI) prediction network presents the ability to quantify the structural damage by the damage patterns and column design parameters.

4. The proposed HysGAN demonstrates the capability to predict damage patterns by effectively utilizing the latent features extracted from the pre-trained HysGRU, thereby facilitating a comprehensive understanding of the damage mechanisms in bridge columns.

5. The HysGAN trained with latent feature condition, RaSGAN loss, and a image resolution 512×512 has the optimal performance, achieving R^2 score 0.98, 0.92, and 0.92 for the generation of training, valdiation, and test data in the damage pattern database.

6. Extensive experimental results have demonstrated that the integration of latent features within HysGAN significantly enhances the image quality and generalizability in predicting damage patterns for unobserved column designs.

In future applications, engineers can access the simulated hysteresis loops by being provided the 17 column features, which encompass material properties, section configurations, and analysis outcomes utilizing the Mander confined concrete model. Subsequently,

doi:10.6342/NTU202402878

by integrating the simulation outcomes, the proposed HysGRU effectively bridges the discrepancy between simulated and experimental results, thereby accurately predicting the hysteresis loops. During the predictive phase, engineers may specify the drift ratio and employ the latent features as conditioning variables for HysGAN. The proposed HysGAN proficiently anticipates the associated damage patterns corresponding to the specified drift ratio and column configuration. By employing the proposed framework, engineers are able to rigorously evaluate the hysteretic response and thoroughly assess the damage mechanisms inherent in the designed bridge columns, leading to more efficient evaluation of seismic design and capacity.

5.2 Limitation and Future Work

As an innovative investigation into the development of a failure prognostic framework for RC bridge columns, the subsequent discussions delineate the potential limitations that require consideration in future research endeavors. We illustrate the limitations through the analysis of two principal tasks, namely the prediction of hysteresis loops and the generation of damage patterns.

- Hysteresis Loop Prediction

    1. The database mainly comprises bridge columns exhibiting flexural failure mechanisms, while data related to columns experiencing flexural-shear and shear failures remain insufficient. Expanding the hysteresis database is imperative to enhance the generalizability of HysGRU.
    2. The current simulation framework primarily takes into account material properties and column geometry. Incorporating a more comprehensive integrated

doi:10.6342/NTU202402878

simulation approach that encompasses a broader range of parameters has the potential to markedly improve the efficacy and predictive accuracy of Hys-GRU.

3. The proposed HysGRU model demonstrates a robust capability in accurately predicting the hysteretic behavior of bridge columns. Nevertheless, it is imperative to undertake a more detailed examination of hysteresis loops to thoroughly assess the seismic characteristics of these columns. In future investigations, the identification of these characteristics during the hysteresis loop prediction may substantially enhance the efficiency of subsequent structural analyses.

- Damage Pattern Generation

1. The currently compiled damage patterns, derived solely from the six column specimens, necessitate the expansion of the damage pattern database to encompass a broader spectrum of column designs, failure modes, and configurations.
2. The proposed HysGAN is able to to forecast the fialure patterns of RC brdige columns. However, the capability only validate on the bridges with flexural failure. In future study, it is imperative to incorporate bridge columns exhibiting flexural-shear and shear failure mechanisms to more comprehensively assess the model performance.
3. In this study, the analysis is confined to the assessment of damage on surfaces oriented parallel to the direction of the applied force, given that the bridge specimens exhibit flexural failure mechanisms. Nonetheless, due to the complexity of the failure mechanisms, it is necessary to extend the data representation into three-dimensional space to model more intricate and realistic damage

doi:10.6342/NTU202402878

scenarios.

4. In practical scenarios, the fracture of longitudinal reinforcements and the displacement of hoop and tie rebars are of greater significance compared to concrete spalling. These critical aspects can be more effectively addressed through the utilization of three-dimensional data that encompasses a more comprehensive depiction of damage scenarios.

doi:10.6342/NTU202402878

References

[1] Ahmed Ghobarah. Performance-based design in earthquake engineering: state of development. Engineering Structures, 23(8):878–884, 2001.

[2] Afsin Saritas and Filip C Filippou. Numerical integration of a class of 3d plastic-damage concrete models and condensation of 3d stress–strain relations for use in beam finite elements. Engineering Structures, 31(10):2327–2336, 2009.

[3] Ying Gao, Junjie Chen, and Liang Zheng. Seismic response and damage analysis of an isolated bridge subjected to near-fault ground motion. Applied Sciences, 12(10): 4878, 2022.

[4] Ping-Hsiung Wang, Kuo-Chun Chang, and Wei-Chung Cheng. Deteriorated hysteresis behaviors of reinforced concrete bridge columns. ACI Structural Journal, 120(2): 33–46, 2023.

[5] Yu-Chen Ou, Si-Huy Ngo, Hwasung Roh, Samuel Y Yin, Jui-Chen Wang, and Ping-Hsiung Wang. Seismic performance of concrete columns with innovative seven-and eleven-spiral reinforcement. ACI Structural Journal, 112(5):579, 2015.

[6] Kuo-Chun Chang, Yu-Chi Sung, Kuang-Yen Liu, Ping-Hsiung Wang, Zheng-Kuan Lee, Lu-Sheng Lee, and Witarto. Seismic performance of an existing bridge with

doi:10.6342/NTU202402878

scoured caisson foundation. Earthquake Engineering and Engineering Vibration, 13:151–165, 2014.

[7] Chris Pantelides, Lawrence Reaveley, Jeffrey Duffin, Jon Ward, and Chris Delahunty. In-situ tests of three bents at south temple bridge on interstate 15–final report. Utah Department of Transportation Research Division. Report No. UT-03.32, Utah, 2003.

[8] Chang Seok Lee and Sang Whan Han. An accurate numerical model simulating hysteretic behavior of reinforced concrete columns irrespective of types of loading protocols. International Journal of Concrete Structures and Materials, 15(1):5, 2021.

[9] Wassim M. Ghannoum and Jack P. Moehle. Dynamic collapse analysis of a concrete frame sustaining column axial failures. ACI Structural journal, 109(3):403, 2012.

[10] M.R. LeBorgne and W.M. Ghannoum. Calibrated analytical element for lateral-strength degradation of reinforced concrete columns. Engineering Structures, 81: 35–48, 2014.

[11] Meijing Hao, Wei Chang, and Wenzhong Zheng. Hysteresis performance and restoring-force model of rc columns jacketed by octagonal and spiral stirrups. Journal of Building Engineering, 82:108280, 2024.

[12] Thomas T. Baber and Yi-Kwei Wen. Random vibration of hysteretic, degrading systems. Journal of the Engineering Mechanics Division, 107(6):1069–1087, 1981.

[13] Thomas T. Baber and Mohammad N. Noori. Random vibration of degrading, pinching systems. Journal of Engineering Mechanics, 111(8):1010–1026, 1985.

[14] Thomas T. Baber and Mohammed N. Noori. Modeling general hysteresis behavior

doi:10.6342/NTU202402878

and random vibration application. Journal of Vibration and Acoustics, 108(4):411–420, 1986.

[15] Ying Ma, Zebin Wu, Xuebin Cheng, Zhiguo Sun, and Xiaoyu Chen. Parameter identification of hysteresis model of reinforced concrete columns considering shear action. In Structures, volume 47, pages 93–104. Elsevier, 2023.

[16] Ian Goodfellow, Yoshua Bengio, and Aaron Courville. Deep learning. MIT press, 2016.

[17] Huan Luo and Stephanie German Paal. Machine learning–based backbone curve model of reinforced concrete columns subjected to cyclic loading reversals. Journal of Computing in Civil Engineering, 32(5):04018042, 2018.

[18] Bilal Ahmed, Sujith Mangalathu, and Jong-Su Jeon. Seismic damage state predictions of reinforced concrete structures using stacked long short-term memory neural networks. Journal of Building Engineering, 46:103737, 2022.

[19] De-Cheng Feng, Barbaros Cetiner, Mohammad Reza Azadi Kakavand, and Ertugrul Taciroglu. Data-driven approach to predict the plastic hinge length of reinforced concrete columns and its application. Journal of Structural Engineering, 147(2): 04020332, 2021.

[20] Chao-Lie Ning, LiPing Wang, and Wenqi Du. A practical approach to predict the hysteresis loop of reinforced concrete columns failing in different modes. Construction and Building Materials, 218:644–656, 2019.

[21] Yajie Miao, Mohammad Gowayyed, and Florian Metze. Eesen: End-to-end speech recognition using deep rnn models and wfst-based decoding. In 2015 IEEE workshop

doi:10.6342/NTU202402878

on automatic speech recognition and understanding (ASRU), pages 167–174. IEEE, 2015.

[22] George Saon, Zoltán Tüske, Daniel Bolanos, and Brian Kingsbury. Advancing rnn transducer technology for speech recognition. In ICASSP 2021-2021 IEEE International Conference on Acoustics, Speech and Signal Processing (ICASSP), pages 5654–5658. IEEE, 2021.

[23] Apeksha Shewalkar, Deepika Nyavanandi, and Simone A. Ludwig. Performance evaluation of deep neural networks applied to speech recognition: Rnn, lstm and gru. Journal of Artificial Intelligence and Soft Computing Research, 9(4):235–245, 2019.

[24] Stefan Kombrink, Tomas Mikolov, Martin Karafiát, and Lukás Burget. Recurrent neural network based language modeling in meeting recognition. In Interspeech, volume 11, pages 2877–2880, 2011.

[25] Tomáš Mikolov, Stefan Kombrink, Lukáš Burget, Jan Černockỳ, and Sanjeev Khudanpur. Extensions of recurrent neural network language model. In 2011 IEEE international conference on acoustics, speech and signal processing (ICASSP), pages 5528–5531. IEEE, 2011.

[26] Aejaz Farooq Ganai and Farida Khursheed. Predicting next word using rnn and lstm cells: Stastical language modeling. In 2019 fifth international conference on image information processing (ICIIP), pages 469–474. IEEE, 2019.

[27] Jun Zhang and Kim-Fung Man. Time series prediction using rnn in multi-dimension embedding phase space. In SMC'98 conference proceedings. 1998 IEEE

doi:10.6342/NTU202402878

international conference on systems, man, and cybernetics (cat. no. 98CH36218), volume 2, pages 1868–1873. IEEE, 1998.

[28] Yao Qin, Dongjin Song, Haifeng Chen, Wei Cheng, Guofei Jiang, and Garrison Cottrell. A dual-stage attention-based recurrent neural network for time series prediction, 2017.

[29] Ibtissam Amalou, Naoual Mouhni, and Abdelmounaim Abdali. Multivariate time series prediction by rnn architectures for energy consumption forecasting. Energy Reports, 8:1084–1091, 2022.

[30] Hyun-Su Kim and Kwang-Seob Park. Research on hyperparameter of rnn for seismic response prediction of a structure with vibration control system. Journal of Korean Association for Spatial Structures, 20(2):51–58, 2020.

[31] Ruiyang Zhang, Zhao Chen, Su Chen, Jingwei Zheng, Oral Büyüköztürk, and Hao Sun. Deep long short-term memory networks for nonlinear structural seismic response prediction. Computers & Structures, 220:55–68, 2019.

[32] Yuchen Liao, Rong Lin, Ruiyang Zhang, and Gang Wu. Attention-based lstm (at-tlstm) neural network for seismic response modeling of bridges. Computers & Structures, 275:106915, 2023.

[33] Hyun-Su Kim. Development of seismic response simulation model for building structures with semi-active control devices using recurrent neural network. Applied Sciences, 10(11):3915, 2020.

[34] Xiangyong Ni, Qingsong Xiong, Qingzhao Kong, and Cheng Yuan. Deep hysteretic-net to predict hysteretic performance of rc columns against cyclic loading. Engineering Structures, 273:115103, 2022.

doi:10.6342/NTU202402878

[35] Salah A Faroughi, Nikhil Pawar, Celio Fernandes, Maziar Raissi, Subasish Das, Nima K. Kalantari, and Seyed Kourosh Mahjour. Physics-guided, physics-informed, and physics-encoded neural networks in scientific computing, 2023.

[36] Yang Liu, Zhu Mei, Bin Wu, Oreste S Bursi, Kao-shan Dai, Bo Li, and Yang Lu. Seismic behaviour and failure-mode-prediction method of a reinforced-concrete rigid-frame bridge with thin-walled tall piers: Investigation by model-updating hybrid test. Engineering Structures, 208:110302, 2020.

[37] T-H Kim, K-M Lee, Y-S Chung, and HM Shin. Seismic damage assessment of reinforced concrete bridge columns. Engineering Structures, 27(4):576–592, 2005.

[38] Ata Babazadeh, Rigoberto Burgueno, and Pedro F. Silva. Use of 3d finite-element models for predicting intermediate damage limit states in rc bridge columns. Journal of Structural Engineering, 141(10):04015012, 2015.

[39] Tarutal Ghosh Mondal and S. Suriya Prakash. Nonlinear finite-element analysis of rc bridge columns under torsion with and without axial compression. Journal of Bridge Engineering, 21(2):04015037, 2016.

[40] A. Mohammed, H. Almansour, and B. Martín-Pérez. Simplified finite element model for evaluation of ultimate capacity of corrosion-damaged reinforced concrete beam-columns. International Journal of Advanced Structural Engineering, 10:381–400, 2018.

[41] Ying Gao, Liang Zheng, Yunshan Han, and Zhiyi Zhao. Damage analysis of reinforced concrete columns based on fiber beam–column element. Applied Sciences, 13(10):6018, 2023.

doi:10.6342/NTU202402878

[42] Ian J. Goodfellow, Jean Pouget-Abadie, Mehdi Mirza, Bing Xu, David Warde-Farley, Sherjil Ozair, Aaron Courville, and Yoshua Bengio. Generative adversarial networks, 2014.

[43] Rahmat Ali and Young-Jin Cha. Attention-based generative adversarial network with internal damage segmentation using thermography. Automation in Construction, 141:104412, 2022.

[44] Seungbo Shim, Jin Kim, Seong-Won Lee, and Gye-Chun Cho. Road damage detection using super-resolution and semi-supervised learning with generative adversarial network. Automation in Construction, 135:104139, 2022.

[45] Mehdi Mirza and Simon Osindero. Conditional generative adversarial nets, 2014.

[46] Gongjie Zhang, Kaiwen Cui, Tzu-Yi Hung, and Shijian Lu. Defect-gan: High-fidelity defect synthesis for automated defect inspection. In Proceedings of the IEEE/CVF Winter Conference on Applications of Computer Vision (WACV), pages 2524–2534, January 2021.

[47] Ting-Yan Wu, Rih-Teng Wu, Ping-Hsiung Wang, Tzu-Kang Lin, and Kuo-Chun Chang. Development of a high-fidelity failure prediction system for reinforced concrete bridge columns using generative adversarial networks. Engineering Structures, 286:116130, 2023.

[48] Young-Ji Park and Alfredo H.-S. Ang. Mechanistic seismic damage model for reinforced concrete. Journal of structural engineering, 111(4):722–739, 1985.

[49] Yang Xu, Yi Li, Xiaohang Zheng, Xiaodong Zheng, and Qiangqiang Zhang. Computer-vision and machine-learning-based seismic damage assessment of reinforced concrete structures. Buildings, 13(5):1258, 2023.

doi:10.6342/NTU202402878

[50] Michael Berry, Myles Parrish, and Marc Eberhard. Peer structural performance database user's manual (version 1.0). University of California, Berkeley, 2004.

[51] Yu-Chen Ou, Jianwei Song, Ping-Hsiung Wang, Leo Adidharma, Kuo-Chun Chang, and George C Lee. Ground motion duration effects on hysteretic behavior of reinforced concrete bridge columns. Journal of Structural Engineering, 140(3): 04013065, 2014.

[52] AASHTO-LRFD bridge design specifications 1st Ed. American Association of State Highway and Transportation Officials, Washington, D.C., 1994.

[53] John B. Mander, Michael J.N. Priestley, and Robert Park. Theoretical stress-strain model for confined concrete. Journal of structural engineering, 114(8):1804–1826, 1988.

[54] G.A. Chang and John B. Mander. Seismic energy based fatigue damage analysis of bridge columns: Part I-Evaluation of seismic capacity. National Center for Earthquake Engineering Research Buffalo, NY, 1994.

[55] Dawn Ellen Lehman. Seismic performance of well-confined concrete bridge columns. University of California, Berkeley, 1998.

[56] Seismic design criteria version 2.0. California Department of Transportation, Sacramento, CA, 2019.

[57] M.J. Nigel Priestley, Frieder Seible, and Gian Michele Calvi. Seismic design and retrofit of bridges. John Wiley & Sons, 1996.

[58] Minjie Zhu, Frank McKenna, and Michael H. Scott. Openseespy: Python library for the opensees finite element framework. SoftwareX, 7:6–11, 2018.

doi:10.6342/NTU202402878

[59] Frank McKenna. Opensees: a framework for earthquake engineering simulation. Computing in Science & Engineering, 13(4):58–66, 2011.

[60] Kyunghyun Cho, Bart van Merrienboer, Caglar Gulcehre, Dzmitry Bahdanau, Fethi Bougares, Holger Schwenk, and Yoshua Bengio. Learning phrase representations using rnn encoder-decoder for statistical machine translation, 2014.

[61] Diederik P. Kingma and Jimmy Ba. Adam: A method for stochastic optimization, 2017.

[62] Alexia Jolicoeur-Martineau. The relativistic discriminator: a key element missing from standard gan, 2018.

[63] Alexey Dosovitskiy, Lucas Beyer, Alexander Kolesnikov, Dirk Weissenborn, Xiaohua Zhai, Thomas Unterthiner, Mostafa Dehghani, Matthias Minderer, Georg Heigold, Sylvain Gelly, Jakob Uszkoreit, and Neil Houlsby. An image is worth 16x16 words: Transformers for image recognition at scale, 2021.

[64] Jia Deng, Wei Dong, Richard Socher, Li-Jia Li, Kai Li, and Li Fei-Fei. Imagenet: A large-scale hierarchical image database. In 2009 IEEE conference on computer vision and pattern recognition, pages 248–255. Ieee, 2009.

[65] Thomas Cover and Peter Hart. Nearest neighbor pattern classification. IEEE transactions on information theory, 13(1):21–27, 1967.

[66] Adam Paszke, Sam Gross, Francisco Massa, Adam Lerer, James Bradbury, Gregory Chanan, Trevor Killeen, Zeming Lin, Natalia Gimelshein, Luca Antiga, Alban Desmaison, Andreas Kopf, Edward Yang, Zachary DeVito, Martin Raison, Alykhan Tejani, Sasank Chilamkurthy, Benoit Steiner, Lu Fang, Junjie Bai, and Soumith

doi:10.6342/NTU202402878

Chintala. Pytorch: An imperative style, high-performance deep learning library. In Advances in Neural Information Processing Systems 32, pages 8024–8035. Curran Associates, Inc., 2019.

[67] Martin Heusel, Hubert Ramsauer, Thomas Unterthiner, Bernhard Nessler, and Sepp Hochreiter. Gans trained by a two time-scale update rule converge to a local nash equilibrium. Advances in neural information processing systems, 30, 2017.

[68] Suman Ravuri and Oriol Vinyals. Classification accuracy score for conditional generative models. Advances in neural information processing systems, 32, 2019.

[69] Yan Xiao and Armen Martirossyan. Seismic performance of high-strength concrete columns. Journal of structural Engineering, 124(3):241–251, 1998.

[70] Tomoya Nagasaka. Effectiveness of steel fiber as web reinforcement in reinforced concrete columns. Transactions of the Japan Concrete Institute, 4(1):493–500, 1982.

[71] Minoru Ohue, Hisao Morimoto, Shigeru Fujii, and Shiro Morita. The behavior of rc short columns failing in splitting bond-shear under dynamic lateral loading. Transactions of the Japan Concrete Institute, 7(1):293–300, 1985.

[72] Xiaoshen Zhou, Toshio Satoh, Weishan Jiang, Arata Ono, and Yasushi Shimizu. Behavior of reinforced concrete short column under high axial load. Transactions of the Japan Concrete Institute, 9(6):541–548, 1987.

[73] Abraham C. Lynn, Jack P. Moehle, Stephen A. Mahin, and William T. Holmes. Seismic evaluation of existing reinforced concrete building columns. Earthquake Spectra, 12(4):715–739, 1996.

[74] Zhou Wang, Alan C Bovik, Hamid R Sheikh, and Eero P Simoncelli. Image quality

doi:10.6342/NTU202402878

assessment: from error visibility to structural similarity. IEEE transactions on image processing, 13(4):600–612, 2004.

[75] Christian Szegedy, Vincent Vanhoucke, Sergey Ioffe, Jon Shlens, and Zbigniew Wojna. Rethinking the inception architecture for computer vision. In Proceedings of the IEEE conference on computer vision and pattern recognition, pages 2818–2826, 2016.

doi:10.6342/NTU202402878